



MSc in Physics

Novel Techniques for Fast and Precise Estimation of Qubit Decay Rates

Filippo Leveraro

Supervised by Jacob Hastrup and Morten Kjærgaard

February 2025



Filippo Leveraro

Novel Techniques for Fast and Precise Estimation of Qubit Decay Rates

MSc in Physics, February 2025

Supervisors: Jacob Hastrup and Morten Kjærgaard

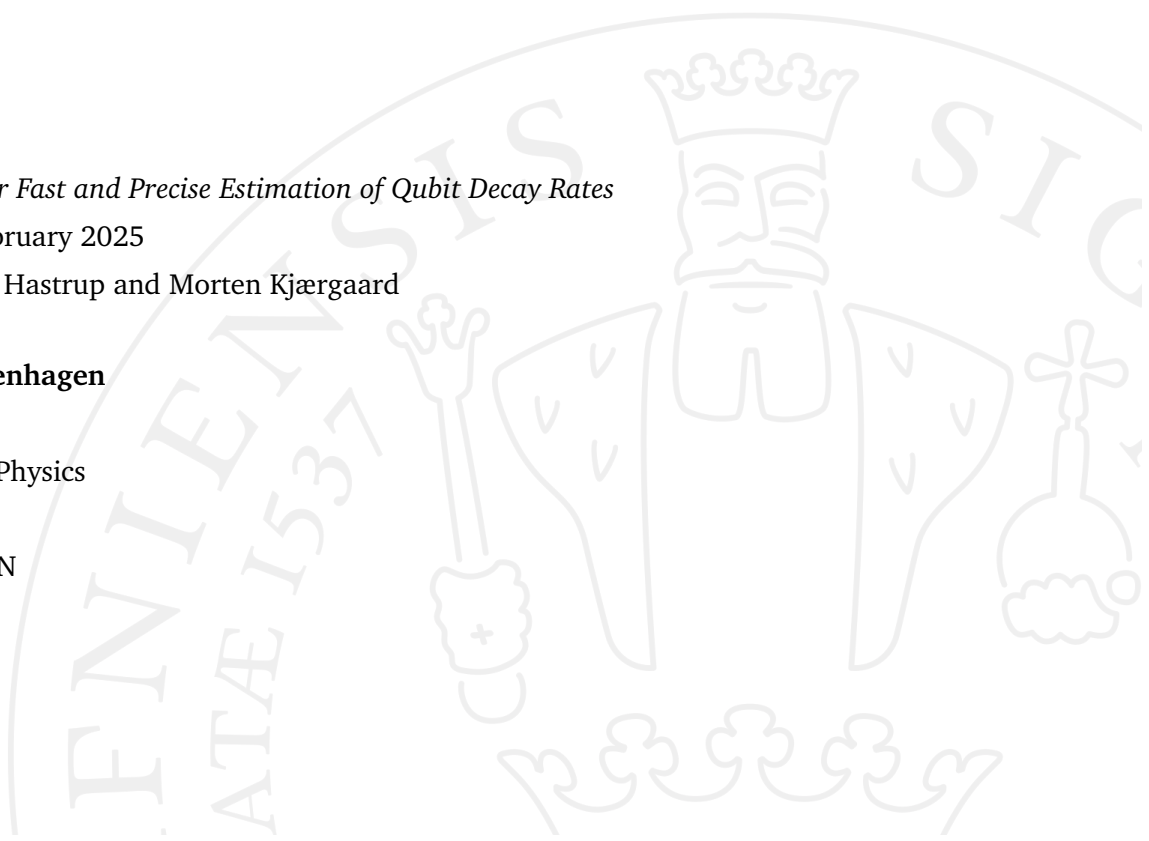
University of Copenhagen

Faculty of Science

Masters Degree in Physics

Blegdamsvej

2200 Copenhagen N



To my grandfathers, "Doviglio" e "Peppone", who recently passed away. Your wisdom, love, and support continue to inspire me every day.

And to my friend Alessandro, who tragically passed away while climbing Mount Legnone in winter. Your adventurous spirit and friendship will always be remembered.

Acknowledgements

Firstly, I would like to express my sincere gratitude to Prof. Morten Kjærgaard for giving me the opportunity to develop an original and unusual thesis that piqued my interests. I am also very grateful to Dr. Lorenzo Leandro for the fantastic opportunity I was presented at Quantum machines, and for bearing with me during the long working hours. Last but not the least, I would like to thank my supervisor Dr. Jacob Hastrup for his infinite patience with my unsatisfactory understanding of the simplest questions that were asked me.

Abstract

This thesis focuses on the difficulties and approaches needed to measure qubit decay rates both quickly and accurately—a fundamental metric in assessing superconducting quantum processors. As one of the leading platforms for scalable quantum computing, superconducting qubits experience decoherence and relaxation phenomena that constrain their performance, especially problematic when trying to scale to size of the system. The primary contribution of this thesis involves creating and deploying a new measurement protocol to improve the efficiency of determining T_1 , the parameter that indicates qubit relaxation time.

A key feature of this research is the integration of continuous, real-time qubit state monitoring with refined statistical methods. This combined strategy negotiates the balance between fast measurements and reliable data, accomplished by fine-tuning experimental timing and minimizing the variance of measurement outcomes.

In addition, this work examines several well-established decay rate measurement techniques, each tailored to different case study, such as fixed-duration experiments with and without active reset. Through numerical simulations and theoretical proofs, these methods are shown to significantly lower the statistical uncertainties associated with T_1 extraction, while at the same time providing the fastest experimental time. The results not only highlight gains in qubit performance assessment but also deepen our understanding of the core physical mechanisms driving qubit relaxation.

Contents

1	Introduction	1
1.1	Thesis Targets	1
2	Introduction to T_1, Measurements, and Lindblad Dynamics	3
2.1	Basics of Quantum Computing	3
2.1.1	Classical Bits vs. Qubits	3
2.1.2	Bloch Sphere Representation	4
2.2	Noise, Decoherence, and Relaxation (T_1)	4
2.2.1	Interactions with the Environment	4
2.2.2	Vertical (Energy) Relaxation: T_1	6
2.3	Two-level system Measurements	7
2.3.1	Generic Measurements Process	7
2.3.2	Two-Level System Case	8
2.3.3	Operations Beyond Measurement	9
2.4	Lindblad Dynamics	10
2.4.1	Vertical Relaxation in the Lindblad Framework	11
3	Quantum Jumps Measurements in SC Qubits	13
3.1	Continuous Measurements in Quantum Jumps	13
3.1.1	Continuous Monitoring with cQED	13
3.1.2	Non-destructive Measurements	14
3.1.3	Weak Gaussian Measurements	14
3.1.4	Transitioning to the Poisson Case	15
3.2	Vijay's Protocol for Observing Quantum Jumps	16
3.3	A Feedback Protocol for Quantum Jumps	18
3.4	Quantum Jumps' Measurements Framework	18
3.4.1	Ansatz Derivation	20
3.4.2	Jump and No-Jump Evolutions	21
3.4.3	Probability Derivation	22
3.5	Inefficient Measurements and SME	23
3.5.1	Noisy Traces Integration	24

3.6	Feedback Control Protocols	25
4	Enhancing Qubit Decay Rate Estimation with Fast Measurements	27
4.1	T_1 : Populations and Probabilities	28
4.2	Standard T_1 Measurement Protocol	29
4.3	Tracking the Qubit State in Real-Time	30
4.4	Exponential Distribution's MLE Derivation	31
4.4.1	Model Statement	31
4.4.2	Asymptotic Variance and Standard Deviation	32
4.4.3	Numerical Verification	33
4.5	Single-Parameter Optimization Solver	33
4.5.1	Fixed experiment time case	36
4.5.2	Reset Time Case	37
4.6	3-Parameter Optimization Solver	39
4.6.1	Reset Time Case	44
5	Conclusions and Outlook	49
6	Bibliography	51

Introduction

Quantum computing is quickly becoming a growing domain in computational science, promising breakthroughs in cryptography, materials discovery, and solving intricate computing challenges. Within the wide range of technologies under development, superconducting qubits have probably got a strong push due to their potential for large-scale development and compatibility with already established manufacturing methods. These type of qubits, which are based on principles of superconductivity and quantum mechanics, are at the base of the fundamental components of quantum processors. However, their performance is often limited by decoherence, an unavoidable phenomenon where quantum information is partly lost through interactions with the surrounding environment.

A fundamental part of decoherence is energy relaxation, measured by the thermal relaxation time, T_1 . This parameter represents the average duration for which a qubit remains in its excited state before falling to its ground state. In this sense T_1 is a key for evaluating qubit quality and reliability, i.e. the quality of quantum information. However, achieving accurate measurements of T_1 is not easy, as it requires careful advanced equilibrium between precision and speed—both of which are essential for practical scaling in quantum technologies.

1.1 Thesis Targets

This thesis focuses on developing novel strategies to enhance the efficiency of T_1 decay rate estimations. The motivation behind these strategies comes from the related fluctuations of T_1 , which can change over time – and across different frequencies. Such fluctuations are frequently attributed to two-level system (TLS) defects, i.e. localized states in the qubit's environment that intermittently absorb and release energy. Understanding the impact of these defects is key to building scalable quantum architectures, which in turn

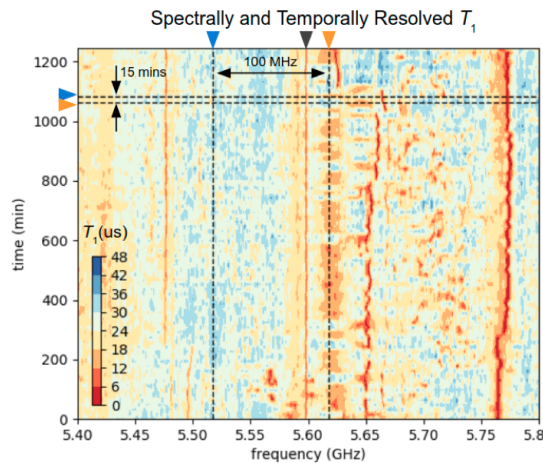


Figure 1.1: Spatially and temporally resolved T_1 fluctuations observed by Klimov et al. in a flux tunable qubit [6]

underlines the importance of robust and swift T_1 measurement techniques [6].

The work presented here has its roots in the framework of circuit quantum electrodynamics (cQED). By leveraging cQED capabilities of measurements, this research introduces innovative approaches for T_1 measurements, combining real-time qubit state monitoring with advanced statistical methods. Such techniques aim to optimize the often competing requirements of measurement speed and fidelity, surpassing the limitations of standard protocols.

The thesis also delves into the theoretical analysis of qubit dynamics under continuous measurements, showing the relationship between quantum jumps and T_1 decay with various derivations. Through numerical simulations and analytical models, scenarios that are not easy to implement experimentally can be explored, offering a deeper view of the trade-offs of T_1 estimation.

Overall, this thesis contributes to the broader objective of robust qubit characterization, laying a path toward developing scalable quantum processors, and scalable characterization processes. As the quantum computing field progresses, rapid and precise T_1 measurements will remain indispensable for advancing device performance and size.

The following chapters outline the theoretical foundations of quantum jumps and T_1 dynamics, introduce the new measurement protocols proposed, and verify their efficacy through derivations and simulations.

Introduction to T_1 , Measurements, and Lindblad Dynamics

In this chapter, we introduce the basics for discussing relaxation time and its dynamics, as well as other phenomena involving qubit systems, particularly in the context of quantum jumps. To do so, it is important to recall the basic definition of a qubit, how it is represented geometrically, and how noise and the surrounding environment can lead to degradation of the qubit state, i.e. quantum information over time. We then introduce the concept of vertical relaxation, which is the core topic of this thesis, and also commonly referred to as energy relaxation or T_1 relaxation time. Then we'll briefly discuss how these processes can be modeled using the density matrices and the Lindbladian, to determine the dynamics of our system.

2.1 Basics of Quantum Computing

2.1.1 Classical Bits vs. Qubits

Traditional (classic) computing is based on the concept of bits, which can take the discrete values 0 or 1, building information upon that, in what is known as binary system. In contrast, a quantum bit, i.e. the qubit, is a two-level quantum system that can exist in any superposition of the logical states $|0\rangle$ and $|1\rangle$. Mathematically, the state of a qubit can be written as [13]

$$|\psi\rangle = \alpha |0\rangle + \beta |1\rangle, \quad \text{where } \alpha, \beta \in \mathbb{C}, \quad |\alpha|^2 + |\beta|^2 = 1. \quad (2.1)$$

where the normalization condition $|\alpha|^2 + |\beta|^2 = 1$ ensures that the total probability of measuring the qubit in state $|0\rangle$ or $|1\rangle$ sums to unity, i.e. 100% of the cases.

The fact that a qubit can be in a continuum of superposed states (not just $|0\rangle$ or $|1\rangle$) is what allows quantum computing to deliver significant computational advantages compared to classical systems. However, this same feature also makes qubits more susceptible to unwanted interactions with the environment, leading to decoherence and relaxation processes [13].

2.1.2 Bloch Sphere Representation

A particularly useful way to visualize a single qubit we just introduced is via what's called the Bloch sphere. With this method, it is possible to represent a pure qubit state $|\psi\rangle$ as a point on the surface of a unitary sphere. In spherical coordinates, which is an easier way to represent a point on a sphere, we can write the previously introduced qubit in terms of [12]

$$|\psi(\theta, \phi)\rangle = \cos\left(\frac{\theta}{2}\right) |0\rangle + e^{i\phi} \sin\left(\frac{\theta}{2}\right) |1\rangle, \quad (2.2)$$

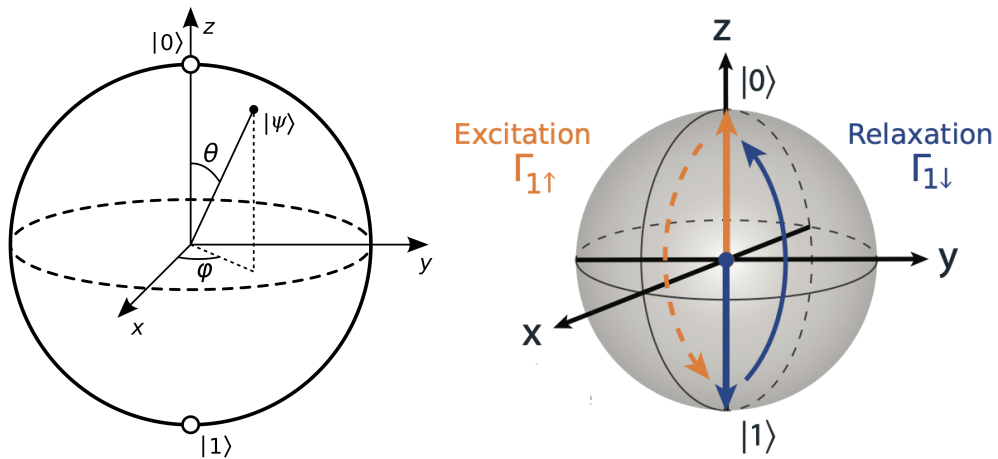
where θ is the polar angle measured from the north pole, which corresponds to $|0\rangle$, and ϕ is the azimuthal angle on the equatorial plane of the sphere. In spherical coordinates, the boundaries $0 \leq \theta \leq \pi$ and $0 \leq \phi < 2\pi$ also need to be respected.

In general, every pure state can be visualized on the Bloch sphere as a point on the surface. Mixed states which are states for which we do not have complete information or equivalently that represent statistical ensembles, can still be represented in this framework but correspond to points inside the Bloch sphere rather than on its surface, i.e. bypassing the normalization condition [12].

2.2 Noise, Decoherence, and Relaxation (T_1)

2.2.1 Interactions with the Environment

In an ideal, perfectly isolated quantum system, a qubit prepared in a whatever state $|\psi(\theta, \phi)\rangle$ would remain in that state for an infinite time. However, real



(a) Bloch sphere representation in spherical coordinates. Credits: Wikipedia [12] (b) Relaxation process visualized on the Bloch sphere. Credits: Krantz et al. [7] (edited)

physical qubits, such as those implemented in our lab, are inevitably coupled and affected by various environmental degrees of freedom [7]. These interactions give rise to different type of errors [7]: *Systematic errors*, which are often due to imperfect control system, imperfect calibration of operations, or unwanted residual couplings, and *Stochastic errors*, such as thermal noise or random fluctuations in the environment.

As we previously mentioned, these noise sources reduce the fidelity of quantum operations and cause the qubit to lose its initial state information over time. Two important timescales to characterize the qubit's loss of information over time are [7]:

1. *Decoherence time* (T_2), related to the loss of phase information (transverse relaxation) in the qubit state.
2. ***Relaxation time* (T_1), related to energy exchange with the environment, typically causing the qubit to decay from the excited state $|1\rangle$ to the ground state $|0\rangle$.**

For the purposes of this thesis, we will focus only on *relaxation* (T_1) and will not address decoherence (T_2) in detail, even though further studies including it can help improve the quality of our novel methods.

2.2.2 Vertical (Energy) Relaxation: T_1

Energy relaxation, which is also known as *vertical relaxation* in Bloch sphere terms due to its visualization, corresponds to transitions between the state $|0\rangle$ and $|1\rangle$. On the Bloch sphere, a decay from $|1\rangle$ to $|0\rangle$ can be pictured as a downward motion from the north pole, which corresponds to the excited state, to the south pole, which corresponds to the ground state [12].

In more formal quantum mechanics terms, these processes can be described using Lindblad jump operators [8]. We will talk about them more specifically later on, but we briefly introduce them now to understand T_1 . Specifically, for a single qubit interacting with a thermal bath at a finite temperature, we can define the jump operators as

$$L_{\downarrow} = \sqrt{\Gamma_{\downarrow}} |0\rangle \langle 1|, \quad L_{\uparrow} = \sqrt{\Gamma_{\uparrow}} |1\rangle \langle 0|, \quad (2.3)$$

where Γ_{\downarrow} is the downward decay rate from $|1\rangle$ to $|0\rangle$ and Γ_{\uparrow} is the upward excitation rate from $|0\rangle$ to $|1\rangle$ [8].

Thermal excitations can on the other side push the system from $|0\rangle$ to $|1\rangle$, competing with the "natural" decay, so that the total *energy relaxation rate* can be written as

$$\Gamma_1 = \Gamma_{\downarrow} + \Gamma_{\uparrow}, \quad (2.4)$$

and the characteristic relaxation time can be written as its inverse

$$T_1 = \frac{1}{\Gamma_1}. \quad (2.5)$$

This T_1 time represents the average timescale on which the excited state population decays due to both decay and thermal excitation effects. In practice, improving Γ_1 (reducing it), and thus T_1 (increasing it), is an ongoing challenge in device engineering and materials science. From the quantum information and control perspective, we can measure and model these processes to design error mitigation methods and optimize measurements, which we will introduce now.

2.3 Two-level system Measurements

So far, we have implicitly considered *pure* states, where the state of the system is perfectly known, i.e. a point on the Bloch sphere. In reality, due to noises, partial measurements, or lack of complete information, quantum states are often described more accurately by *mixed* states, i.e. points inside the sphere. One way to handle these situations is via the density matrix (or density operator), which we'll introduce following manzano et al. [8]. A general quantum state can be written as a combination of pure states, such as

$$\rho = \sum_i p_i |\psi_i\rangle \langle\psi_i|, \quad \text{where } \sum_i p_i = 1 \text{ and } p_i \geq 0. \quad (2.6)$$

here the newly introduced density matrix ρ must satisfy two conditions: $\text{Tr}(\rho) = 1$, i.e. normalization, and $\rho \geq 0$, i.e. positivity.

A complete discussion of quantum dynamics and Hilbert spaces is beyond our immediate target, but it is important to clarify how measurements are described and applied to the specific case of T_1 measurements. I.e., whenever we speak of *knowing the state* of the system, we assume that an experimental procedure has been performed to measure that state. Therefore, we must understand both how we can carry out measurements and how the act of measurement itself affects the quantum state, and more in general our system.

2.3.1 Generic Measurements Process

Measurements in quantum mechanics are represented (and performed) by what's known as *observables*, which mathematically are Hermitian operators acting on the system's Hilbert space. A general observable M can be written in its spectral form as

$$M = \sum_i a_i |a_i\rangle \langle a_i|, \quad (2.7)$$

where a_i are the eigenvalues of the observable M , and $|a_i\rangle$ are the corresponding normalized eigenvectors [8].

When the system is in a pure state $|\psi\rangle$, the probability of obtaining a particular eigenvalue a_i upon measurement is given by the square module of the

projection of the state on the eigenstate corresponding to the eigenvalue as [8]

$$P(a_i) = |\langle a_i | \psi \rangle|^2. \quad (2.8)$$

Immediately after the measurement that yields the result a_i , the system collapses -in the projective measurement sense- to the corresponding eigenstate $|a_i\rangle$. In other words, the post-measurement state can be written as [8]

$$|\psi_{\text{post}}\rangle = \frac{|a_i\rangle \langle a_i | \psi \rangle}{\sqrt{P(a_i)}}. \quad (2.9)$$

Let's now put this aside, because as said before, mixed states are more relevant for our T_1 case analysis. To consider also mixed states in our definition, it is possible to generalize the previous statement, and rewrite the probability as the trace of [8]

$$P(a_i) = \text{Tr}\{|a_i\rangle \langle a_i | \rho\}. \quad (2.10)$$

This definition will be useful later on to define the probability of certain outcomes in quantum jumps. Before applying it to a more complicated scenario, we first try to use it in a simple system like the one suggested in the next paragraph.

2.3.2 Two-Level System Case

We now focus on the two-level system that is relevant to qubit physics and T_1 measurements. Following the derivation in Manzano et al. [8], let us now consider the measurement operator

$$H = E_0 |0\rangle \langle 0| + E_1 |1\rangle \langle 1|, \quad (2.11)$$

where E_0 and E_1 are the eigenvalues corresponding to the basis states $|0\rangle$ and $|1\rangle$, respectively. Assume the state to be measured is defined as

$$|\psi\rangle = \alpha |0\rangle + \beta |1\rangle, \quad \text{with} \quad |\alpha|^2 + |\beta|^2 = 1. \quad (2.12)$$

In this system, the probability of measuring E_0 , i.e., finding the system in $|0\rangle$ is given by $P(E_0) = |\alpha|^2$, while respectively, the probability of measuring E_1 , i.e., finding the system in $|1\rangle$ will be $P(E_1) = |\beta|^2$.

This simple two-level example shows how measurement probabilities in a two-level system are directly determined by the amplitude coefficients of the superposition state. For T_1 measurements, one typically tracks the probability of finding the qubit in the ground state $|0\rangle$ (energy E_0) as a function of time, thereby extracting the characteristic decay time of the excited state population [8]. We will talk further about T_1 measurement protocols in the next chapter.

2.3.3 Operations Beyond Measurement

Until now, our discussion has mainly concerned the measurement of a quantum state. However, to perform a wide range of manipulations (including novel methods introduced later in this thesis), one must also apply operations other than measurements. In a typical qubit implementation, these operations can be visualized as rotations on the Bloch sphere. This is one of the reasons why the density matrix proves so useful: any rotation on the sphere can be expressed as a matrix, i.e. an operator, acting on the density matrix itself. We will not delve into the details, but we need to differentiate between different transformations, so that we know the conditions they imply.

A common basis for such transformations involves the Pauli matrices, which allow one to construct any rotation or, in general, any unitary transformation. We can generally distinguish between two classes of transformations [8]:

Unitary transformations, which preserve the probability amplitudes, i.e., $|\alpha|^2 + |\beta|^2 = 1$ remain true, which indicates that no information is lost to the environment. These transformations describe the evolution of an *isolated* quantum system [8].

Non-unitary transformations on the other side, do not conserve the state normalization in the same way, reflecting processes where information is lost to the environment. Such transformations can lead to mixed states and prevent the exact recovery of the original state. Dissipative effects,

including relaxation and decoherence, are modeled by this non-unitary dynamics [8].

In the context of T_1 measurements, understanding non-unitary transformations is crucial because they capture the key dissipation processes that cause population decay or excitation in a two-level system. So let us now apply this knowledge to an open quantum system, in order to understand its dynamics when environment and measurements interfere with it.

2.4 Lindblad Dynamics

With the density matrix formalism we previously introduced, useful to handle pure and mixed states, a strategy for measurement, and the notion of applying transformations, we are now equipped to describe the evolution of an open quantum system. Following Manzano et al. [8], an open quantum system interacting with its environment is governed by the so-called *Lindblad master equation*. This equation extends the closed-system Schrödinger equation by including interaction terms that model energy exchange and decoherence processes due to interaction with the local environment. In short, the master equation evolves the density matrix ρ while accounting for dissipative effects. The Master Equation reads [8]:

$$\frac{d\rho}{dt} = -\frac{i}{\hbar} [H, \rho] + \sum_k \left(L_k \rho L_k^\dagger - \frac{1}{2} \{L_k^\dagger L_k, \rho\} \right). \quad (2.13)$$

Here, the Hamiltonian term governs the *unitary* (closed-system) evolution, as for in the Schrödinger equation, while the second sum term incorporates all relevant *dissipative* effects through the so-called *Lindblad jump operators* L_k . These operators include processes such as relaxation and decoherence by describing the system's coupling to external degrees of freedom [8].

From the standpoint of T_1 measurements, the dissipative part of the Lindblad equation is particularly important, as it is responsible for transitions between $|0\rangle$ and $|1\rangle$. As we described earlier, jump operators model upward and downward transitions, which together define the energy relaxation rate for the qubit. In principle, it is also possible to introduce additional Lindblad operators to model other phenomena such as thermalization or dephasing.

For our purposes, we will focus on jump processes corresponding to two-level dissipation, since these alone suffice to model T_1 relaxation in a qubit.

2.4.1 Vertical Relaxation in the Lindblad Framework

Having introduced the necessary tools for describing open quantum systems, in the specific case of vertical relaxation, we can now analyze it in the Lindblad formalism. Recalling from earlier discussions that the overall relaxation rate can be written as

$$\Gamma_1 = \Gamma_{\downarrow} + \Gamma_{\uparrow},$$

where Γ_{\downarrow} denotes the decay rate from $|1\rangle$ to $|0\rangle$, and Γ_{\uparrow} denotes the corresponding excitation rate from $|0\rangle$ to $|1\rangle$. Within this framework, we define the Lindblad jump operators as:

$$L_{\downarrow} = \sqrt{\Gamma_{\downarrow}} |0\rangle\langle 1|, \quad L_{\uparrow} = \sqrt{\Gamma_{\uparrow}} |1\rangle\langle 0|.$$

When these jump operators act on the density matrix $\rho(t)$, the equation governing the system's dynamics can be written as

$$\dot{\rho}(t) = \mathcal{D}[L_{\downarrow}]\rho(t) + \mathcal{D}[L_{\uparrow}]\rho(t), \quad (2.14)$$

where $\mathcal{D}[L]$ represents the Lindblad dissipator¹ [8]. We will not focus on the detailed steps of solving these equations; instead, we note that for a two-level system (i.e., a 2×2 density matrix), one can solve the corresponding set of differential equations to find $\rho(t)$.

As an illustrative example, the population of the ground state $|0\rangle$, denoted by $\rho_{00}(t)$, follows an exponential behavior [8]:

$$\rho_{00}(t) = \frac{\Gamma_{\downarrow}}{\Gamma_1} + \left[\rho_{00}(0) - \frac{\Gamma_{\downarrow}}{\Gamma_1} \right] e^{-\Gamma_1 t}. \quad (2.15)$$

¹For an operator L , the dissipator is typically defined as

$$\mathcal{D}[L]\rho = L\rho L^\dagger - \frac{1}{2}\{L^\dagger L, \rho\}.$$

The other matrix elements exhibit similar exponential dependencies, reflecting the balance between relaxation and excitation processes. What is important to remember here is that all the elements of the density matrix have an exponential dependency. In general, we operate with low-temperature experiment setups, where thermal excitations are strongly suppressed ($\Gamma_{\uparrow} \approx 0$), which implies $\Gamma_1 \approx \Gamma_{\downarrow}$. Under such conditions, the qubit's excited-state population primarily decays toward $|0\rangle$, yielding the well-known exponential decay form central to T_1 measurements [1].

Quantum Jumps Measurements in SC Qubits

3.1 Continuous Measurements in Quantum Jumps

Quantum jumps, which are transitions observed in quantum systems, have been a fundamental concept in quantum mechanics since their first postulation. In the context of superconducting qubits, these jumps are particularly significant as they provide insights into quantum measurement processes and the intrinsic dynamics of qubits relaxation, which is the focus of this work. following, we try to explain the nature of quantum jumps, and the continuous measurement protocol we need to apply to monitor them in real-time. To do that, we'll focus on key experiments by Vijay et al. [11] and elaborates on the derivation from the Lindblad master equation to quantum jumps of Jordan and Siddiqi [4]. We will also make use of Jacobs et al. [2] to introduce the framework for continuous measurements, and Jordan et al. [5] for in depth derivations.

3.1.1 Continuous Monitoring with cQED

The circuit quantum electrodynamics (cQED) architecture offers an elegant solution for continuous monitoring. By detuning the frequency of the qubit and cavity, it is possible to continuously probe the dynamics without destroying the qubit state. The microwave photons resulting from qubit transitions are not emitted into free space but are efficiently coupled into a one-dimensional waveguide, which is connected to a superconducting parametric amplifier [4].

3.1.2 Non-destructive Measurements

We just named "without destroying the qubit state", which is also known as the concept of *continuous* or *weak* measurements. While the standard T_1 experiment protocol involves a sequence of prepare-and-measure steps where each measurement projects (and thereby destroys) the current state, our goal now is to consider measurement schemes that extract information more gently, so that we leave the qubit state partially intact. This weaker measurement scheme will be an enabling key for the novel methods developed in the following chapter.

Let us now suppose we wish to measure the qubit state without causing a full projective collapse. Such non-destructive measurements require that the coupling between the measurement apparatus and the qubit to be sufficiently weak, so the qubit remains coherent, i.e. information is not completely lost. In return, the measurement outcome provides only partial information about the state [2].

We then need to introduce a parameter s that characterizes the *strength* of the measurement, representing the information extraction rate in a given time interval Δt , as we repeat the measurement for a certain amount of time: if $s = 0$ it implies that *no* information is acquired (no coupling), and the qubit state remains completely untouched. If $s = 1$, it corresponds to a projective measurement, yielding maximal information but fully collapsing the state. Intermediate values $0 < s < 1$ thus represent weak measurements that strike a balance between preserving coherence and gaining information

3.1.3 Weak Gaussian Measurements

To start, let's consider a continuous variable x that is being observed with Gaussian resolution, having mean α and variance determined by $s\Delta t$. During a short time interval Δt , the relevant measurement operator can be written as [2]

$$\Omega_g(\alpha) = \left(\frac{4s\Delta t}{\pi}\right)^{1/4} \int dx \exp[-2s\Delta t(x-\alpha)^2] |x\rangle\langle x|, \quad (3.1)$$

where $|x\rangle$ are eigenstates of the (continuous) observable x . The exponential factor indicates a Gaussian weighting centered at $x = \alpha$. This operator form will be relevant in subsequent chapter when we describe a specific realization of continuous measurement in qubit systems [2].

3.1.4 Transitioning to the Poisson Case

We know that jump statistics is not Gaussian, i.e. continuous but Poissonian, i.e. discrete, as the event itself manifests as an improvised "jump". So we can say that a Poissonian measurement protocol, can well capture zero, a single or multiple events in it's statistic. So in this case we can consider a discrete variable n and suppose that in the interval Δt , the average number of detection is $\gamma\Delta t$, i.e. γ is the detection rate. In this case, it is possible to define the measurement operator as

$$\Omega_p(n) = \sqrt{\frac{(\gamma\Delta t)^n e^{-\gamma\Delta t}}{n!}} |n\rangle \langle n| \quad (3.2)$$

where $|n\rangle$ are the eigenstates of the discrete variable. Let's notice that we lost s in this transition. That is because in this case γ implicitly dictates how "strong" the measurement is, as higher γ means "more jumps", i.e. more opportunities for the system to collapse into the "jumped" state. The observable acts on the state, driving it towards a new state. In this "jump", it is more interesting talking about probabilities, as the state will stay the same or jump. In Poissonian probability, if γ is the detection rate, then in a small interval of time Δt we can say that the probability of detecting no event in the $t + \Delta t$ timeframe is approximately

$$p_0 \approx e^{-\gamma\Delta t} \quad (3.3)$$

that for small Δt can be expanded as $p_0 = 1 - \gamma\Delta t + \mathcal{O}(\Delta t^2)$. Equivalently, if in that timeframe one event has occurred, then the probability, in case of small timeframes, can be written as $p_j \approx \gamma\Delta t$, excluding higher orders. These results will be useful later on, when will apply them to Lindbladian dynamics.

3.2 Vijay’s Protocol for Observing Quantum Jumps

In 2011, Vijay et al.[11] developed an experiment with the purpose of observing these quantum jumps in a transmon qubit. This has been done by continuously monitoring the emission of the qubit, and associating them to quantum jumps.

As illustrated in Figure 3.1a [11], the process of detecting these quantum jumps begins by driving the qubit with a brief resonant pulse, pushing it into its excited state. Subsequently, a projective measurement of the qubit is performed by sending the photons through a cavity. The microwave signal leaving the cavity picks up a phase shift dependent on whether the qubit is excited or not. This phase-sensitive signal is then captured, and a mixer translates the high-frequency oscillations recorded into a constant voltage for analysis.

Displayed in Figure 3.1b [11] are three representative voltage traces. Two of these follow a π -pulse, which excites the qubit, while the third trace results from a 2π -pulse, returning the system to the ground state. Under steady conditions, a low voltage reading corresponds to the qubit’s ground state. However, a π -pulse initially drives the voltage to a higher level, characteristic of the excited state, before it swiftly settles back to the ground state value—a clear indication of a quantum jump.

A steady, low-voltage output signifies that the qubit is in its ground state. When π pulses are applied, the voltage quickly rises, reflecting the qubit’s transition to the excited state, before dropping back to the ground-state level—an event that indicates a quantum jump. As seen in Figure 3.2a, the duration of time the qubit remains excited decays exponentially, mirroring the lifetime measured in a standard T_1 sequence [4].

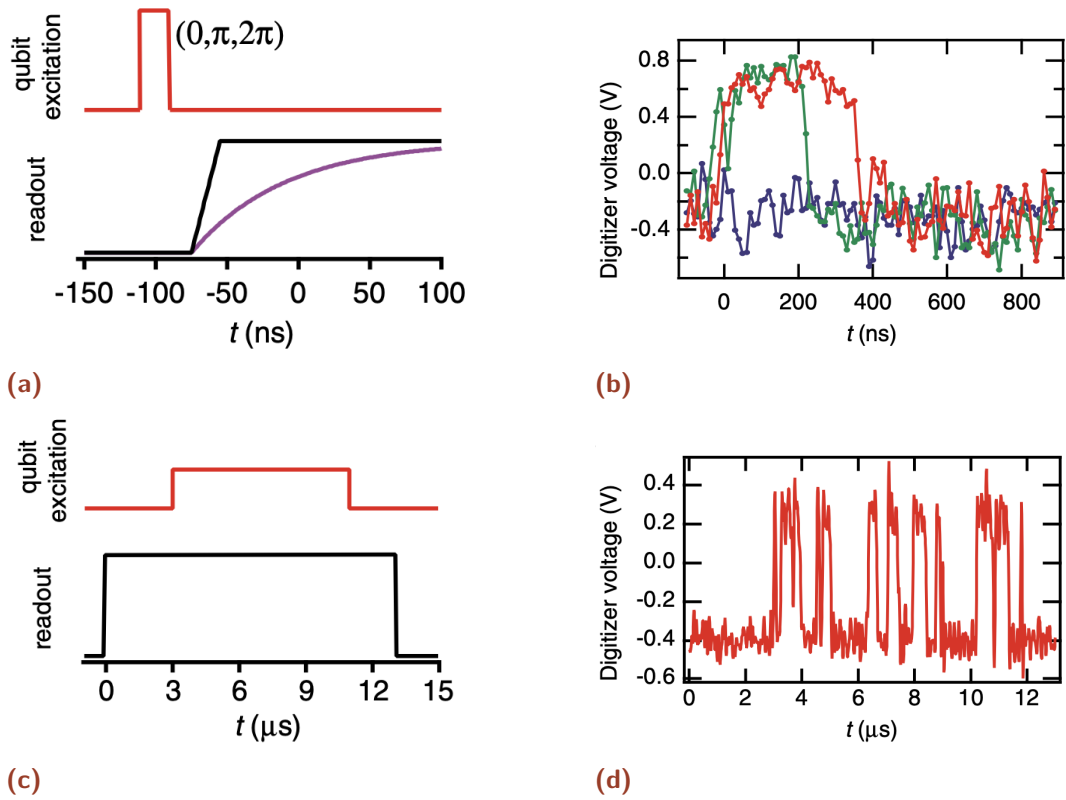


Figure 3.1: (a) The pulse sequence used to generate single shot measurement traces. (b) Voltage output showing quantum jumps following a π (red and green) and 2π (blue) pulse. (c) The pulse sequence used to readout. (d) A single trace of the qubit jumping between the ground and excited state. [11]

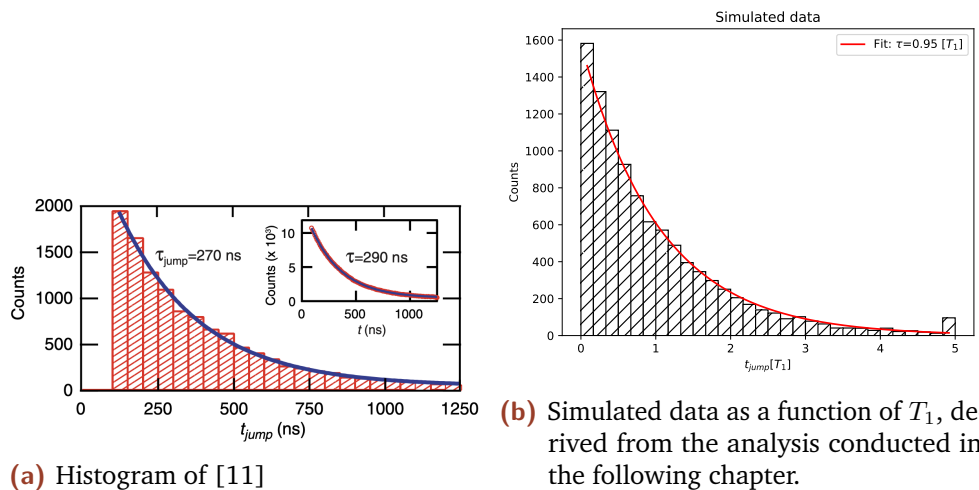


Figure 3.2: Histograms of jump times from the excited state to the ground state extracted from individual measurements.

3.3 A Feedback Protocol for Quantum Jumps

Recent advancements in quantum control protocols have allowed for not only the observation of quantum jumps but also their manipulation. Mineev et al. [9] leveraged advanced quantum control to reveal the continuous nature of quantum jumps.

The experiment involved two superconducting transmon qubits strongly coupled to create a V system with a ground state $|G\rangle$ and two excited states $|B\rangle$ and $|D\rangle$ [9]. The $|B\rangle$ state is strongly coupled to the environment (bright state), and the $|D\rangle$ state is isolated (dark state). The transition to the $|B\rangle$ state causes a significant shift in the cavity frequency, allowing for effective detection of the $|B\rangle$ state while leaving $|D\rangle$ undisturbed. This configuration enabled continuous monitoring of quantum jumps.

The continuous monitoring and control were facilitated by a complex feedback loop, enabling the experimenters to suppress or enhance specific transitions. The setup effectively utilized the Quantum Zeno Effect, where frequent measurements inhibited the transition between states, effectively "freezing" the system in its current state [4].

3.4 Quantum Jumps' Measurements Framework

To understand quantum jumps from a theoretical perspective, we start with the previously introduced Lindblad master equation [8], which describes the time evolution of the density matrix ρ of an open quantum system:

$$\frac{d\rho}{dt} = -i[H, \rho] + \mathcal{L}[\rho], \quad (3.4)$$

where H is the system Hamiltonian and \mathcal{L} is the Lindbladian superoperator. The Lindbladian can be written as [8]:

$$\mathcal{L}[\rho] = \sum_j \left(L_j \rho L_j^\dagger - \frac{1}{2} \{L_j^\dagger L_j, \rho\} \right), \quad (3.5)$$

where L_j are the Lindblad operators representing different decoherence channels. We can now transition to the formalism for quantum jumps.

In the previous section, the master equation was derived under the assumption of both Gaussian and Poisson statistics, where respectively a continuous or discrete variable is measured. However, jump statistics are not Gaussian but Poissonian. As we said, Poisson statistics naturally describe quantum jumps, since they give the probability for a certain number of events to occur at a rate γ within a time interval dt [4].

Assume that $dt \ll \gamma^{-1}$, so that the observation timescale is much shorter than the characteristic timescale of the events. Recalling that the density matrix evolves according to

$$\rho_{final} = \frac{\Omega \rho \Omega^\dagger}{\text{Tr}(\Omega \rho \Omega^\dagger)} \quad (3.6)$$

with Ω as the measurement operators, we see that there are two possible outcomes for the system: a jump event or a no-jump evolution [4]. Then the density matrix will evolve accordingly to some specific measurement operators Ω_0 (no jump) and Ω_j (jump) as [5]

$$\rho \xrightarrow{dt} \begin{cases} \frac{\Omega_0 \rho \Omega_0^\dagger}{\text{Tr}(\Omega_0 \rho \Omega_0^\dagger)} & \text{with probability } p_0 = \text{Tr}(\Omega_0 \rho \Omega_0^\dagger), \\ \frac{\Omega_j \rho \Omega_j^\dagger}{\text{Tr}(\Omega_j \rho \Omega_j^\dagger)} & \text{with probability } p_j = \text{Tr}(\Omega_j \rho \Omega_j^\dagger). \end{cases}$$

Assuming a Lindbladian evolution, the state evolves, if no jump occurs (0 counts), primarily under the Hamiltonian H with a small non-unitary dissipation. A generic strategy to describe the Kraus operator (observable) in this case, is through a suitable ansatz as [4]:

$$\Omega_0 = \mathbb{1} - iHdt + Adt, \quad (3.7)$$

where A is some unknown Hermitian operator¹. Otherwise, in the case of jumps, we can write an observable that scales with time by recalling the probability of a jump and defining the probability condition

$$p_j = \text{Tr}[\Omega_j \rho \Omega_j^\dagger] \quad (3.8)$$

the Kraus operator for the jump can be written as [4]:

$$\Omega_j = \sqrt{dt} L_j \quad (3.9)$$

3.4.1 Ansatz Derivation

Even though we defined the operators, we also need to find the missing part of the ansatz, i.e. A . By imposing the unitary condition

$$\Omega_0^\dagger \Omega_0 + \sum_{j=1} \Omega_j^\dagger \Omega_j = \mathbb{I},$$

we can find the form of the unknown operator A as in Jordan et al [5]. To do it, let's recall the ansatz we provided just above in the previous paragraph:

$$\Omega_0 = \mathbb{I} - iH dt + Adt, \quad (3.10)$$

$$\Omega_j = \sqrt{dt} L_j, \quad (3.11)$$

Substituting these forms into the unitary condition we just defined, we can determine $\Omega^\dagger \Omega$ for the two separate terms of the equation, discarding all the higher order terms in dt as [5]

¹Hermitian so to provide correct normalization and consistency with the Linblad form

$$\Omega_0^\dagger \Omega_0 = (\mathbb{I} + iH dt + A dt) (\mathbb{I} - iH dt + A dt) \quad (3.12)$$

$$\approx \mathbb{I} + iH dt - iH dt + 2A dt = \mathbb{I} + 2A dt, \quad (3.13)$$

Equivalently, for the jump operators Ω_j :

$$\sum_j \Omega_j^\dagger \Omega_j = \sum_j (\sqrt{dt} L_j)^\dagger (\sqrt{dt} L_j) = \sum_j dt L_j^\dagger L_j = dt \sum_j L_j^\dagger L_j. \quad (3.14)$$

Then the unitary condition becomes

$$(\mathbb{I} + 2A dt) + dt \sum_j L_j^\dagger L_j = \mathbb{I}, \quad (3.15)$$

which implies (to first order in dt)

$$2A dt + dt \sum_j L_j^\dagger L_j = 0 \implies A = -\frac{1}{2} \sum_j L_j^\dagger L_j. \quad (3.16)$$

Then expanding Eq. 3.4 to first order in dt , it is possible to find the two distinct classes of evolution [4], using the two kraus operators we just found.

3.4.2 Jump and No-Jump Evolutions

The no-jump (nj) evolution corresponds to the deterministic part of the Lindblad equation we provided above, given by [4]:

$$\rho^{nj}(t + dt) = \rho^{nj} - i[H, \rho] - \frac{dt}{2} \{\rho, \sum_j L_j^\dagger L_j\} + dt \sum_j \text{Tr}(L_j^\dagger L_j \rho) \rho \quad (3.17)$$

This part of the equation represents the smooth, continuous evolution of the quantum state under the influence of the Hamiltonian H and the dephasing effects introduced by the environment [4].

If a jump occurs (j), the state of the system is projected by one of the Lindblad operators L_j , and the density matrix is updated as [4]:

$$\rho^j = \frac{L_j \rho L_j^\dagger}{\text{Tr}(L_j^\dagger L_j \rho)}. \quad (3.18)$$

The probability of a jump occurring in a short time interval dt is proportional to dt , and the state evolution can be described by a stochastic Schrödinger equation. Combining these results, we can describe the dynamics of quantum jumps using a precise deterministic process, where the system evolves deterministically between jumps and stochastically updates upon a jump [4].

3.4.3 Probability Derivation

As in the previous paragraph we derived the formulas for the measurement operators Ω_0 and Ω_j , as well as the the evolutions dynamics in two cases, we can then determine the probability with which each of these scenarios occur. Above we defined the no-jump probability as $p_0 = \text{Tr}(\Omega_0 \rho \Omega_0^\dagger)$ in the timeframe $(t + dt)$. Recalling that the result of the operation $\Omega_0^\dagger \Omega_0$ in the limit $dt \rightarrow 0$ is

$$\Omega_0^\dagger \Omega_0 = \mathbb{I} - dt \sum_j L_j^\dagger L_j \quad (3.19)$$

and using the cycling property, we find that

$$p_0 = \text{Tr}[\rho \Omega_0^\dagger \Omega_0] \approx \text{Tr}\left[\rho \left(\mathbb{I} - dt \sum_j L_j^\dagger L_j\right)\right] = 1 - dt \sum_j \text{Tr}[L_j^\dagger L_j \rho]. \quad (3.20)$$

We can then say that the probability of no-jump during time interval dt is [4]:

$$P_{nj} = 1 - \sum_j \text{Tr}(L_j^\dagger L_j \rho) dt. \quad (3.21)$$

Equivalently, recalling that we defined the jump measurement operator as $\Omega_j = \sqrt{dt} L_j$, the probability of observing a jump then becomes

$$p_j = \text{Tr}[\Omega_j \rho \Omega_j^\dagger] = \text{Tr}[dt L_j \rho L_j^\dagger] = dt \text{Tr}[L_j \rho L_j^\dagger]. \quad (3.22)$$

and then the probability of a jump occurring is given by [4]:

$$P_j = \text{Tr}(L_j^\dagger L_j \rho) dt. \quad (3.23)$$

Thus, the state of the system after time interval dt can be summarized as [4]:

$$\rho(t + dt) = \begin{cases} \frac{L_j \rho L_j^\dagger}{\text{Tr}(L_j^\dagger L_j \rho)} & \text{with probability } P_j, \\ \rho - dt \left(i[H, \rho] + \frac{1}{2} \sum_j \{L_j^\dagger L_j, \rho\} \right) & \text{with probability } P_{nj}. \end{cases} \quad (3.24)$$

3.5 Inefficient Measurements and SME

Beyond measurement strength s , or measurement rate γ , there is often an *efficiency* factor η that captures how much of the emitted signal is actually detected. In many experimental setups, not all the available information reaches the detector. This situation can be modeled by what's known as the *stochastic master equation*, or SME in short, which generalizes the standard master equation previously introduced by including noise terms that represent partial measurement outcomes. The stochastic master equation reads [2],

$$d\rho = -i[H, \rho] dt + \mathcal{D}[c] \rho dt + \eta \mathcal{H}[c] \rho dW, \quad (3.25)$$

where H is the system Hamiltonian, c are the jump (or collapse) operators relevant to the case we are trying to study, $\mathcal{D}[\cdot]$ denotes the usual Lindblad

dissipator we defined in the previous chapter, $\mathcal{H}[\cdot]$ is a superoperator capturing the measurement backaction on the qubit, dW is a what's called the Wiener increment, and $\eta \in [0, 1]$ is the measurement efficiency. This last term is the one we are going to analyze more in-depth in this section.

In this way, η interpolates between situations where all measurement records are perfectly acquired ($\eta = 1$) and where only a fraction of the signal is detected ($\eta < 1$).

This formalism for continuous, weak and inefficient measurements for detecting quantum jumps will form the basis for the method proposed in later chapter, wherein we try to use partial, non-destructive readout measurements to track the qubit state and characterize energy relaxation in real-time. For now, let's just try to put this in action, to try to understand how it works in our quantum jumps case.

3.5.1 Noisy Traces Integration

To calculate the jump times from the excited state to the ground state, which we extract from individual measurements, we must first process the so-called raw traces. These traces, which represent the voltage output showing quantum jumps, are often dominated by noise, making the signal difficult to distinguish at first glance (as illustrated in Figure 3.1). Our simulation of this scenario, previously shown in Figure 3.2b, highlights the importance of accurately determining these jump times.

To simulate the raw traces, we solve the stochastic master equation using QuTiP[3] for a two-level quantum system. This approach incorporates two types of collapse operators: \mathcal{C}_i and \mathcal{S}_n . The first set, \mathcal{C}_i , represents environmental dissipation, while the second set, \mathcal{S}_n , corresponds to monitoring operators. For our two-level system, the relevant collapse operators are $c_1 = \sqrt{\Gamma_1}\sigma_-$ and $c_2 = \sqrt{\kappa}a$, where σ_- is the lowering operator that transitions the state from $|1\rangle$ to $|0\rangle$, and a (or σ_+) is the raising operator that transitions the state from $|0\rangle$ to $|1\rangle$.

Our monitoring operator, $s_1 = \sqrt{\eta}\sigma_z$, projects our measurement onto the $|0\rangle$ and $|1\rangle$ states with an efficiency η . By simulating this system, we generate a

noisy trace, which corresponds to the simulated measured signal (Figure 3.3). The significant level of noise in the trace is immediately apparent, suggesting that the method and length of integration play a crucial role in generating a clean trace from which accurate jump times can be extracted.

While the choice of thresholding method also influences the results, this discussion will focus on the integration process. To determine the optimal integration window, we perform multiple integrations on the same measured signal, generating different binary traces for each integration window. From these traces, we extract the T_1 times by analyzing individual decay events and plotting the results (Figure 3.4, left plot). This analysis allows us to identify the best integration window for processing noisy traces.

Furthermore, we investigate how varying the measurement efficiency η affects the signal. The efficiency parameter η acts as a measure of the signal's clarity; increasing η results in a cleaner trace before integration. Consequently, a cleaner initial trace reduces the impact of the integration window on the final clean trace, which we use to determine T_1 values. This effect is clearly visible in Figure 3.4, right plot, where higher efficiencies correspond to a broader optimal integration window.

3.6 Feedback Control Protocols

Quantum control protocols play a crucial role in manipulating quantum jumps. Advanced techniques allow for the precise control of qubit states, enabling the suppression or enhancement of quantum jumps. These protocols are essential for quantum error correction and the development of robust quantum computing systems.

Feedback control involves real-time adjustments to the system based on measurement outcomes. In the context of quantum jumps, feedback control can be used to suppress unwanted transitions or to stabilize desired states. This approach is crucial for maintaining the coherence of qubits in a quantum processor.

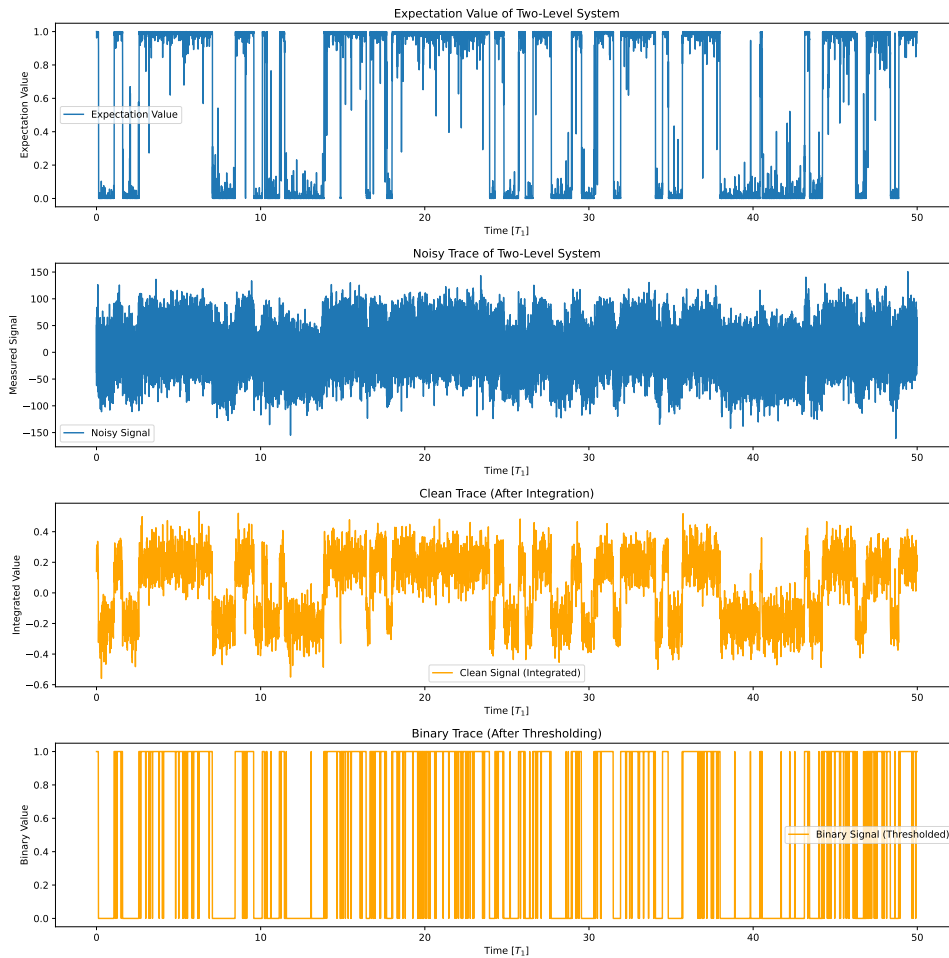


Figure 3.3: From top to bottom: The expectation value of the stochastic master equation; the simulated noisy trace representing the voltage output showing quantum jumps; the clean signal obtain by integration of the noisy trace; the binary trace, obtained as mean value threshold of the clean signal.

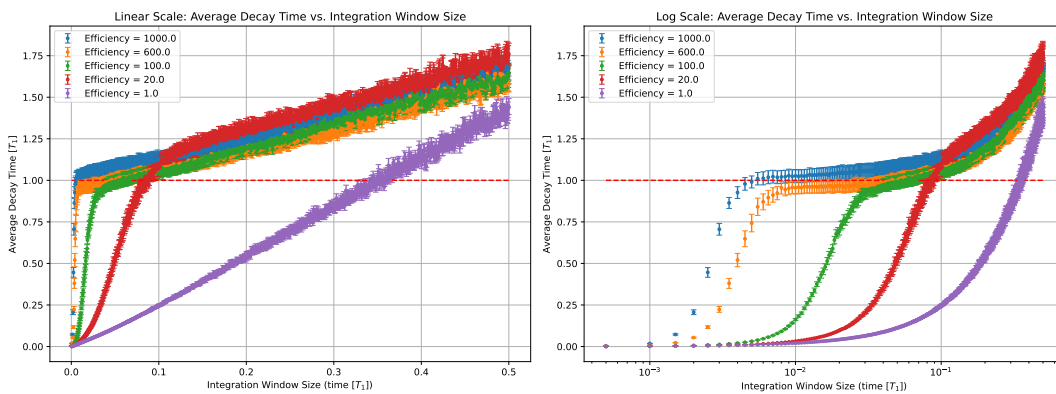


Figure 3.4: (Left) Linear plot showing extracted T_1 times as a function of different integration windows for different measurement efficiency η . (Right) Logarithmic scale plot illustrating the impact of varying measurement efficiencies η on the optimal integration window. The optimal integration window is identified where the T_1 values stabilize. Higher efficiencies result in a wider range of integration windows that yield stable T_1 values.

Enhancing Qubit Decay Rate Estimation with Fast Measurements

The decay of the superposition of quantum states poses a significant limitation to the execution of complex quantum algorithms. This phenomenon, known as quantum decoherence, is typically characterized by measuring two key parameters: T_1 (thermal relaxation time) and T_2 (dephasing time). A major challenge in this field is the stabilization of these energy-relaxation times, which can fluctuate unpredictably over time and frequency. Klimov et al. (2018) [6] utilized qubits as spectral and temporal probes of individual two-level-system (TLS) defects, providing direct evidence that T_1 decays are responsible for the most significant fluctuations.

Numerous studies, including the ones mentioned in the previous chapter, have demonstrated that the largest fluctuations can be attributed to TLS defects and time-dependent variations in their transition frequencies—a phenomenon referred to as spectral diffusion. However, the microscopic nature of TLS defects remains poorly understood. These fluctuations are particularly noteworthy, as T_1 has been shown to vary by up to an order of magnitude, with abrupt changes occurring over 15-minute timescales and across 5 MHz frequencies [6]. Consequently, achieving precise T_1 measurements with minimal uncertainty could provide valuable insights into the underlying phenomena driving qubit relaxation. In this chapter we delve into the mathematical derivation and the numerical simulation of the fastest T_1 measurements, achieving the highest precision (in terms of standard deviation) within the shortest time.

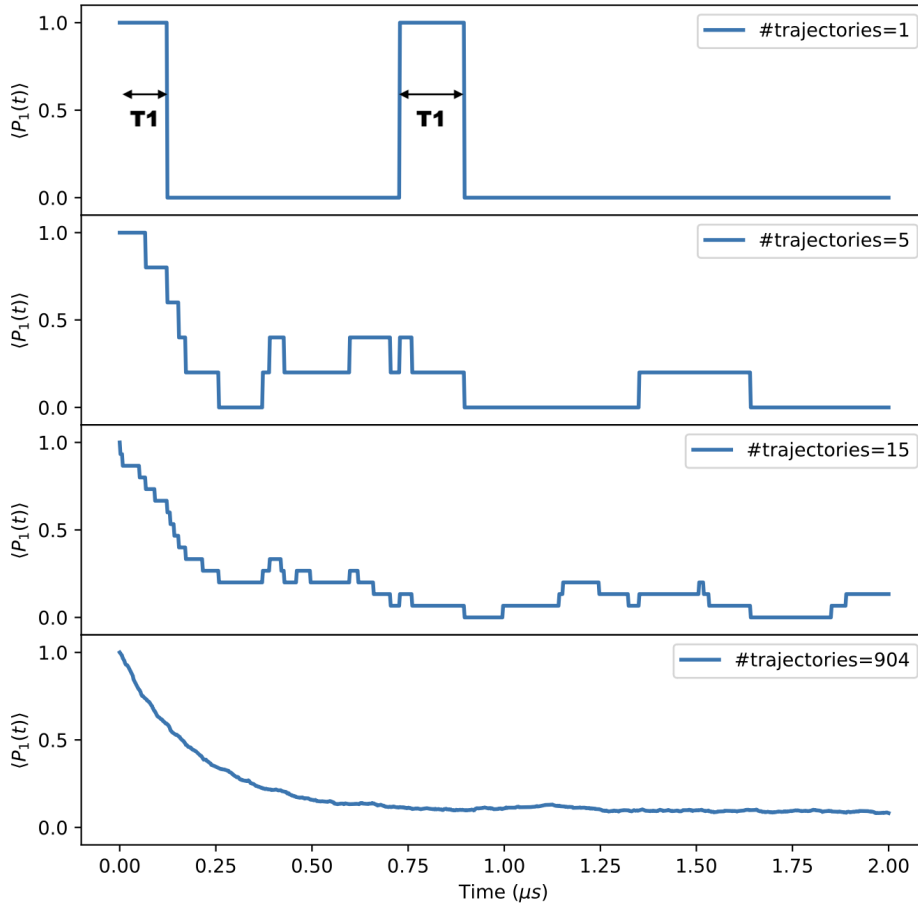


Figure 4.1: The top plot shows a simulated single clean qubit trace as a function of time. The following plots show a set of simulated clean qubit traces (trajectories), averaged 5, 15, and 904 times. The bottom plot shows how the averaging of many trajectories, lead to the exponential decay.

4.1 T_1 : Populations and Probabilities

Thermal relaxation time, T_1 , is defined as the time required for a qubit to transition from the excited state $|1\rangle$ to the ground state $|0\rangle$. This process can be described by the density matrix $\rho = \alpha|\psi\rangle\langle\psi| + \beta|g\rangle\langle g|$, where α is the probability of the qubit being in state $|\psi\rangle$ and β is the probability of the qubit being in the ground state $|g\rangle$. Over time, β approaches 1. Experimentally, T_1 is defined as the time at which the population of the excited state decays to $1/e$ of its initial value, following the relation $P_1(t) = P_1(0)e^{-t/T_1}$.

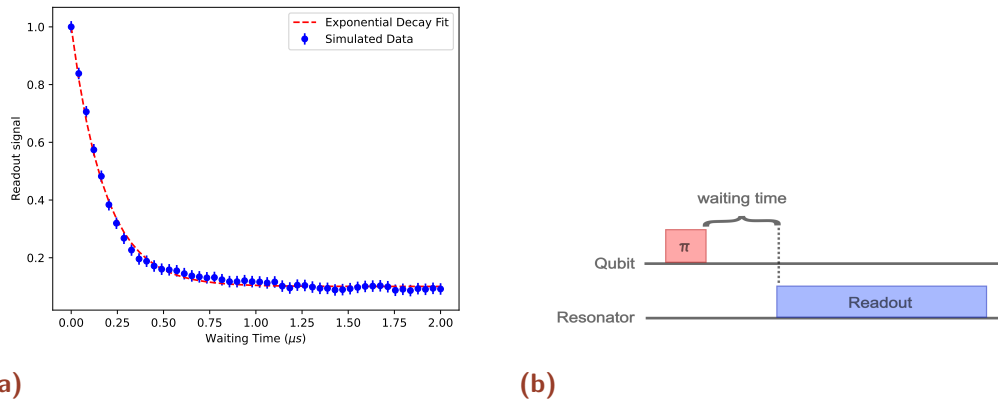


Figure 4.2: Simulated data from an experiment determining a T_1 decay time (a), and the pulse sequence use to do a T_1 experiment (b).

4.2 Standard T_1 Measurement Protocol

Experimentally, the value of T_1 is determined through the following sequence of operations:

1. Prepare the qubit in the excited state by applying a π -pulse.
2. Wait for a specified time t .
3. Measure the state of the qubit (0 or 1).
4. Allow the qubit to thermally reset.
5. Repeat the process for different values of t and average the results at each t .
6. Determine T_1 by fitting an exponential decay curve to the data.

This is similar to flipping a coin: while each individual flip results in either heads or tails, the likelihood of getting heads or tails can be determined by flipping the coin multiple times and calculating the average outcome over all those flips.

It is evident that T_1 measurements are strongly dependent on time, both in terms of the duration required to complete the measurement and the time needed for the qubit to reset to its original state. Different methods of measuring T_1 do not affect its intrinsic value, which is determined by the fabrication and overall experimental setup of the qubit. However, this study aims to emphasize the precision of these measurements, specifically the uncertainty σ with which these measurements are conducted. As discussed, improving the precision of T_1 measurements could provide deeper insights into the physics driving the process and offer a novel method for benchmarking quantum processors. At the same time, it will also provide the fastest measurement of T_1 as with the sequence outlined above, allowing us to better track how T_1 evolves over time.

4.3 Tracking the Qubit State in Real-Time

Assuming continuous monitoring and control as described in Chapter 3, we can observe discrete transitions of a qubit over time, known as quantum jumps. This process, referred to as real-time tracking of the qubit, allows us to know the qubit's state at every point in time. Consider that the signal is an ideal step function, with every trace of noise meticulously eliminated. Additionally, let us assume a perfect and instant feedback system, enabling immediate control and knowledge of the state, and the ability to perform operations instantaneously based on the measurement outcomes. Under these assumptions, we have a system where the qubit can be 'continuously measured,' resulting in a perfect, clean trace with no noise, where transitions between $|0\rangle$ and $|1\rangle$ are clearly distinguishable. From such a trace (Figure 4.3, top), we can measure T_1 by observing the time the qubit remains in state $|1\rangle$ before decaying to $|0\rangle$. Although this method resembles the standard approach for measuring T_1 , it represents a completely different experimental process. To push to the theoretical limits, we assume that every time the qubit state drops to the ground state, we can instantly reset it to its excited state with another π pulse, with no delay (Figure 4.3, bottom). This approach increases the number of T_1 measurements we can obtain from a trace of the same length, as we are continuously collecting information about the system without waiting. While such a system is idealized, it allows us to explore the theoretical limits of our measurements.

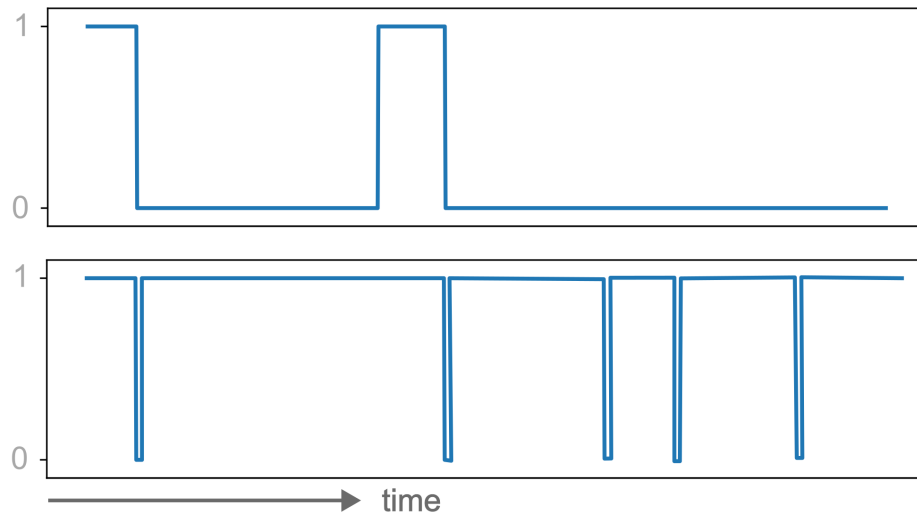


Figure 4.3: Real-time tracking of a qubit state showing discrete transitions, also known as quantum jumps. The top trace represents an ideal clean trace with no noise, allowing clear differentiation between states $|0\rangle$ and $|1\rangle$ (top). The qubit's lifetime in state $|1\rangle$ before decaying to $|0\rangle$ can be measured to determine T_1 . The bottom trace illustrates an idealized system where the qubit is instantly reset to its excited state each time it drops to the ground state, increasing the number of T_1 measurements within the same trace length, i.e. observing time.

4.4 Exponential Distribution's MLE Derivation

In this section, we derive the maximum likelihood estimator of the parameter of an exponential distribution. We do this in order to determine how the uncertainty on the estimated parameter (T_1) scales accordingly to the number of samples taken. We take for granted the maximum likelihood estimation (MLE) theory needed to understand the proofs.

4.4.1 Model Statement

Let X_1, X_2, \dots, X_n be random samples from an exponential distribution with parameter $\gamma > 0$. Experimentally these samples would correspond to the results of the T_1 sequence previously illustrated. Here, instead of fitting the

data, we estimate the parameters of the assumed probability distribution, given a sample. The probability density function (PDF) of X_i is given by [10]:

$$f(x; \gamma) = \begin{cases} \gamma e^{-\gamma x} & x \geq 0, \\ 0 & x < 0. \end{cases}$$

The likelihood function $L(\gamma)$ for the sample is:

$$L(\gamma) = \prod_{i=1}^n \gamma e^{-\gamma x_i} = \gamma^n e^{-\gamma \sum_{i=1}^n x_i}.$$

The log-likelihood function $\ell(\gamma)$ is:

$$\ell(\gamma) = \ln L(\gamma) = n \ln \gamma - \gamma \sum_{i=1}^n x_i.$$

To find the maximum likelihood estimator (MLE) of γ , we take the derivative of $\ell(\gamma)$ with respect to γ and set it to zero:

$$\frac{d\ell(\gamma)}{d\gamma} = \frac{n}{\gamma} - \sum_{i=1}^n x_i = 0.$$

Solving for γ , we obtain:

$$\hat{\gamma} = \frac{n}{\sum_{i=1}^n x_i}. \quad (4.1)$$

4.4.2 Asymptotic Variance and Standard Deviation

The asymptotic variance of the MLE $\hat{\gamma}$ is given by the inverse of the Fisher information [10]:

$$\text{Var}(\hat{\gamma}) = \frac{\gamma^2}{n}. \quad (4.2)$$

which gives a standard deviation of:

$$\text{Std}(\hat{\gamma}) = \frac{\gamma}{\sqrt{n}} \quad (4.3)$$

This demonstrates how the standard deviation of T_1 measurements, represented here by its reciprocal γ , scales with the number of samples n . However,

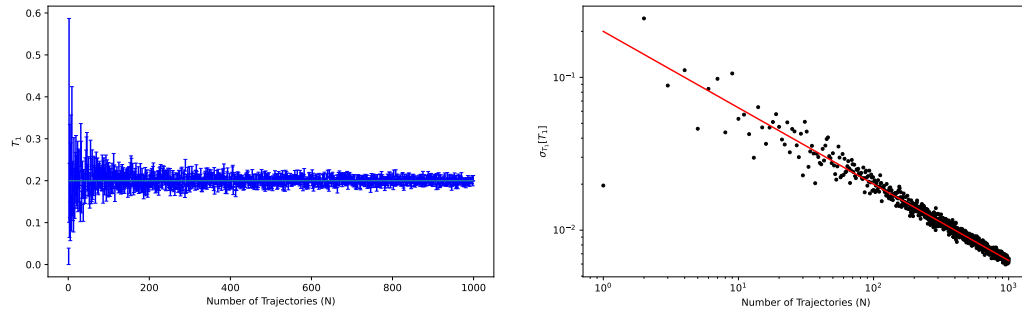


Figure 4.4: Comparison of numerically simulated T_1 measurements with theoretical predictions. The left panel shows the T_1 values obtained from the first decay of multiple trajectories, ensuring that the number of trajectories matches the number of samples. The right panel illustrates the uncertainty in T_1 measurements for increasing number of samples, comparing the numerical results to the analytical solution, demonstrating the alignment between our theory and experimental data.

describing it as a function of n is not particularly effective for our purposes. Since each measurement is taken at a specific time t , the total measurement time is more relevant than the number of samples. Later in this chapter we will reintroduce the standard deviation of T_1 as a function of time.

4.4.3 Numerical Verification

However, we can compare it to some numerically simulated data to demonstrate that our theory aligns with the experiment. For simplicity, instead of generating an actively resetting trace, we generate multiple trajectories and consider one sample per trajectory, specifically the first decay as a T_1 measurement. This approach ensures that the number of trajectories matches the number of samples. We then measure T_1 (Figure 4.4, left) and its uncertainty (Figure 4.4, right) for different number of sample and compare these results to the analytical solution.

4.5 Single-Parameter Optimization Solver

In this section, we will explore another mathematical derivation aimed at determining how the precision of our decay rate measurements, specifically the standard deviation, scales with the number of measurements performed

during an experiment, with a different approach This analysis focuses on the "1-point shot" method, which involves repeated measurements at the same sampling time t . These repeated measurements are averaged to produce a single data point, which is then used to estimate the parameter γ of the exponential distribution:

$$f(x) = \exp[-\gamma x] \quad (4.4)$$

To do this, I want to estimate γ provided an estimate of f at some point x . In particular, I'm interested in determining which x will give the small variance on my estimate of γ . In this equation x corresponds to the sampling time t we discussed above, which is the time at which our points are sampled. Now let the point be (y_0, x_0) . My estimate of γ is found by inverting $f(x)$ as:

$$\gamma = -\frac{\log(y_0)}{x_0} \quad (4.5)$$

The uncertainty on γ is then determined by differentiating Eq. 4.5 as:

$$\partial\gamma = \left| \frac{d}{dy_0} \left(-\frac{\log(y_0)}{x_0} \right) \partial y_0 \right| \quad (4.6)$$

Calculating the derivative, we find:

$$\partial\gamma = \frac{1}{y_0 x_0} \partial y_0 \quad (4.7)$$

Assuming we are measuring a qubit where N is the number of shots, the uncertainty of y in (x_0, y_0) due to binomial statistics is given by:

$$\langle \partial y_0 \rangle = \sqrt{\frac{y_0 - y_0^2}{N}} \quad (4.8)$$

We observe that the uncertainty of the sampled point decreases towards zero as y_0 approaches 0 and 1. This occurs respectively when x_0 approaches inf and

0, which are the limiting cases where we would always measure the qubit in state $|0\rangle$ or $|1\rangle$. Thus, the uncertainty in γ becomes:

$$\langle \partial\gamma \rangle = \frac{\sqrt{y_0 - y_0^2}}{y_0 x_0 \sqrt{N}} = \frac{1}{x_0 \sqrt{N}} \sqrt{y_0^{-1} - 1} \quad (4.9)$$

By inserting $y_0 = f(x_0)$, we get:

$$\langle \partial\gamma \rangle = \frac{1}{x_0 \sqrt{N}} \sqrt{\exp[\gamma x_0] - 1} \quad (4.10)$$

This expression describes the evolution of the uncertainty on the exponential parameter as function of the number of samples N , and the sampling time x_0 . Now we want to minimize this expression to obtain the lowest uncertainty possible. To find the optimal sampling point x_0 that minimizes the uncertainty in γ , we solve the equation:

$$\frac{d}{dx} \langle \partial\gamma \rangle = 0 \quad (4.11)$$

The optimal x_0 is found to be:

$$x_{\text{opt}} = \frac{\text{LambertW}(-2 \exp(-2)) + 2}{2\gamma} \quad (4.12)$$

Where the Lambert W function, also known as the product logarithm, is a set of functions, defined as the inverse relation of $f(w) = we^w$.

Approximately, the optimal value is:

$$x_{\text{opt}} \approx 0.795\gamma^{-1} \quad (4.13)$$

Using Eq. 4.10, the minimal uncertainty in γ is then:

$$\langle \partial\gamma \rangle_{\text{opt}} = \frac{\gamma}{0.795\sqrt{N}} \sqrt{\exp[0.795] - 1} \approx 1.386 \frac{\gamma}{\sqrt{N}} \quad (4.14)$$

This result, which expresses the lowest achievable uncertainty as a function of the number of samples, presents a challenge. Specifically, our optimization was based on a fixed number N of samples. However, each measurement is inherently time-dependent, as it is conducted at specific sampling interval. Therefore, it is more appropriate to introduce a time-dependent description rather than one based solely on the number of samples. Let's explore this scenario in more detail.

4.5.1 Fixed experiment time case

In order to solve the problem depicted above, we have to define a new parameter for the total experimental time, T . We now fix the total experiment time to be $T = Nx_0$, thus $N = \frac{T}{x_0}$. Then, the new expression for $\langle \partial\gamma \rangle$ (Eq. 4.10) is given by:

$$\langle \partial\gamma \rangle = \frac{1}{x_0\sqrt{\frac{T}{x_0}}} \sqrt{\exp(\gamma x_0) - 1} = \frac{1}{\sqrt{x_0 T}} \sqrt{\exp(\gamma x_0) - 1} \quad (4.15)$$

Repeating the same optimization previously performed through Eq. 4.11, we try to determine the best sampling time x_0 to minimize $\langle \partial\gamma \rangle$. In this case, $\langle \partial\gamma \rangle$ does not have a local minimum with respect to x_0 . The optimal strategy becomes to take samples with as small x_0 as possible (Figure 4.6a). In the limit as $x_0 \rightarrow 0$, we have:

$$\langle \partial\gamma \rangle \rightarrow \frac{1}{\sqrt{x_0 T}} \sqrt{\gamma x_0} = \frac{\sqrt{\gamma}}{\sqrt{T}} \quad (4.16)$$

Thus, in the limit of $x_0 \rightarrow 0$, $\langle \partial\gamma \rangle$ simplifies to $\frac{\sqrt{\gamma}}{\sqrt{T}}$, indicating that the precision of the measurement improves as the total sampling time T is increased. This result is equivalent to Eq. 4.3¹, reducing this case to the limit of MLE. We'll

¹in the case where $x_0 \approx 1/\gamma$

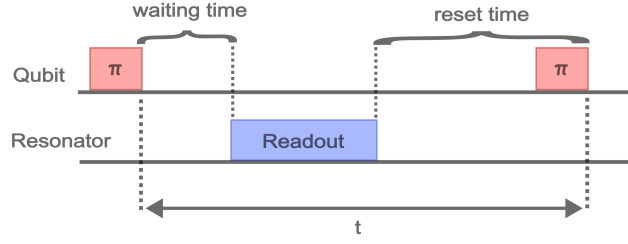


Figure 4.5: Pulse sequence used to perform a T_1 experiment, emphasizing the modeled parameter t .

refer to these as 'instant measurements', as there's no time lost in between each measurement.

4.5.2 Reset Time Case

The limit of perfect measurements, i.e. instant measurements, is quite a case limit, seeing no real applications in experiments. To introduce delays given by different factors, such as reset time, or readout time, we introduce a new parameter t to the equation:

$$T = N(x_0 + t) \quad (4.17)$$

where t is the generic term for a time delay between a measurement and the other. This can be for example the active reset time, to actively reset the qubits to their original state, imagining we have a feedback control system that can perform real-time adjustments to the system based on measurement outcomes, or alternatively, a wait time to passively reset it, or others. This time parameter is purely a generic factor, and can include whatever process can be included between following measurements. I.e. $t = t_{\text{reset}} + \dots + t_{\text{readout}}$. Providing this substitution in terms of x_0 to Eq. 4.10, then Eq. 4.11 reads:

$$\frac{T x_{\text{opt}}^2 \sqrt{\frac{t+x_{\text{opt}}}{T x_{\text{opt}}^2}} \cdot \left(\frac{1}{2T x_{\text{opt}}^2} - \frac{t+x_{\text{opt}}}{T x_{\text{opt}}^3} \right) \sqrt{e^{\gamma x_{\text{opt}}} - 1}}{t + x_{\text{opt}}} + \frac{\gamma \sqrt{\frac{t+x_{\text{opt}}}{T x_{\text{opt}}^2}} e^{\gamma x_{\text{opt}}}}{2\sqrt{e^{\gamma x_{\text{opt}}} - 1}} = 0 \quad (4.18)$$

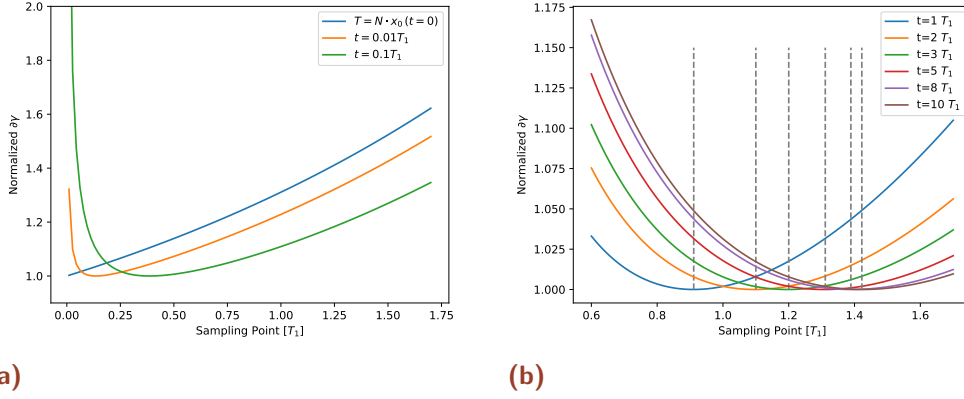


Figure 4.6: (a) The optimization curve for the fixed experiment time with $t = 0$ (blue), showing no minimum compared to solutions with small t . (b) Set of normalized curves for the fixed experiment time with reset time, showing the shift of the peak for the optimized sampling point.

Multiplying this equation by \sqrt{T} eliminates the dependence on the total time, providing valuable insight into the optimal sampling points for T_1 measurements to minimize their standard deviation, given a time interval t between measurements. Although there is no analytical solution to this equation, numerical solutions reveal a local minimum. This local minimum shifts towards higher optimal times, x_{opt} , as the interval t increases (Figure 4.6b). This suggests that the exponential curve should be sampled at longer times when the interval between measurements increases.

We can now visualize the spacing between these results to determine which method yields better T_1 measurements, specifically aiming for a smaller standard deviation given the same total experimental time T (figure 4.7). Compared to the previously shown MLE solution, we now plot all the solutions in terms of total experimental time instead of the number of trajectories. This approach is taken because the sampling time dictates how many measurements can be conducted within that timeframe. As previously discussed, the MLE solution is equivalent to the analytical single-point solution in the simplified case where $t = 0$. As we expected, these different single-point solutions result in the same scaling of our σ_{T_1} , but with some offset between them. To illustrate this, we plot the results, splitting the solution parameterized by t into two cases. The first case is defined as active reset, where we fix $t = 0.01T_1 \equiv t_{\text{reset}}$. This approach aims to demonstrate how active reset, i.e. short delay times, compares to our first Maximum Likelihood Estimation (MLE) solution, which assumes perfect measurements with $t = 0$. In an active reset protocol, the

qubit is reset to its excited state after the observed decay. More frequently, due to the advanced performance and knowledge required to track and reset the qubit and the necessity for high-quality quantum control platforms, researchers resort to passive reset. In passive reset, a certain amount of time is allowed for the qubit to thermally reset (cool) itself. In our example, we set $t = 10T_1 \equiv t_{\text{wait}}$, eliminating the need for direct manipulation of the qubit. This approach is more practical and commonly implemented in experimental setups. To verify our theoretical solutions, we turn to simulations. The first step in this process involves obtaining our sampling point. We achieve this by generating a series of binary choices (0 or 1) at the optimized sampling point x_{opt} , with the probability of these choices derived from the assumed exponential distribution evaluated at that point as

$$p = f(x_{\text{opt}}) = \exp(-\gamma x_{\text{opt}}) \quad (4.19)$$

$$\begin{cases} |0\rangle, & \text{with probability } 1 - p \\ |1\rangle, & \text{with probability } p \end{cases} \quad (4.20)$$

By averaging these binary choices, we obtain the single-shot point in x_{opt} . This single-shot point allows us to fit the exponential distribution from which we sampled. Through this fitting process, we can determine the exponential parameter and its associated uncertainty. This method ensures that our theoretical models are accurately represented and validated through empirical data.

4.6 3-Parameter Optimization Solver

Previously, we assumed a perfect exponential distribution characterized by a single parameter. This assumption is quite strong and does not account for other possible effects. To conduct a more comprehensive study, we now consider a three-parameter exponential function. The improved exponential decay function is given by:

$$f(x) = A \exp[-Bx] + C \quad (4.21)$$

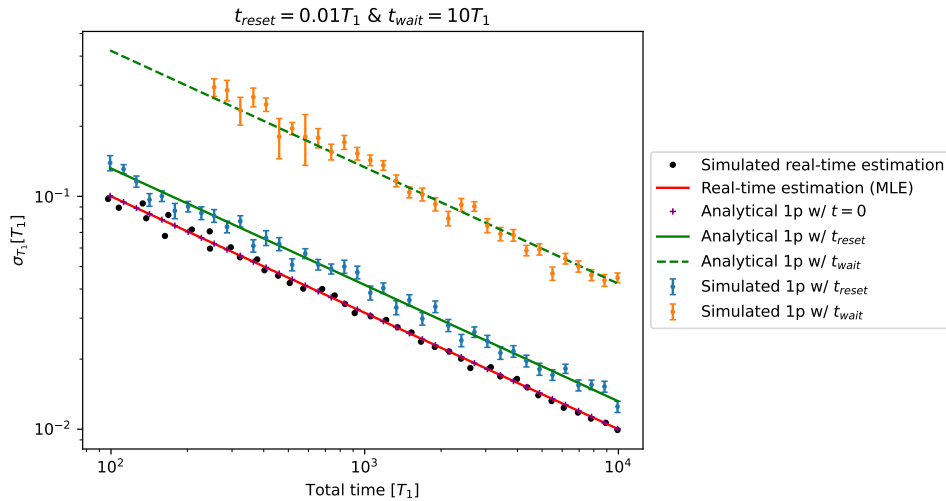


Figure 4.7: Comparison of T_1 measurement methods, visualizing the spacing between different approaches to determine which yields better T_1 measurements with a smaller standard deviation given the same total experimental time T . The results show that all solutions have the same scaling for σ_{T_1} , but with different offsets. The plot includes two cases parameterized by t . The first case, active reset, fixes $t = 0.01T_1 \equiv t_{\text{reset}}$, illustrating how active reset (short delay times) compares to the Maximum Likelihood Estimation (MLE) solution, and the single shot solution assuming perfect measurements with $t = 0$. In active reset protocols, the qubit is reset to its excited state after decay. In passive reset, the qubit is allowed to thermally reset over time, with $t = 10T_1 \equiv t_{\text{wait}}$ in this example, avoiding direct manipulation of the qubit.

where B is the parameter whose uncertainty we are interested in, analogous to γ in our previous calculations.

To determine the parameters A , B , and C of the curve, we need to establish new initial conditions. Since one point is insufficient to determine three parameters, we require three points instead. Let these points be $y_i = f(x_i)$ for $i = \dots 0, 1, 2$. Then:

$$y_i = A \exp[-Bx_i] + C \quad (4.22)$$

Let's now try to isolate the parameter B in the exponential. First, we eliminate C by considering the differences between the function values at different points as:

$$y_0 - y_1 = A(\exp[-Bx_0] - \exp[-Bx_1]) \quad (4.23)$$

$$y_1 - y_2 = A(\exp[-Bx_1] - \exp[-Bx_2]) \quad (4.24)$$

Next, we eliminate A by taking the ratio of the above equations:

$$\frac{y_0 - y_1}{y_1 - y_2} = \frac{\exp[-Bx_0] - \exp[-Bx_1]}{\exp[-Bx_1] - \exp[-Bx_2]} \quad (4.25)$$

Now we need to solve for B . Since an analytical solution to this equation appears to be unavailable, a numerical approach is necessary. However, our primary interest is not in determining the value of B itself, but in calculating its standard deviation. Solving the equation numerically would not provide analytical insights into how the standard deviation scales with time. To achieve this, we need to change our perspective and focus on directly determining the uncertainty of B using a different approach, rather than the standard approach of calculating B .

Similar to the one-point solution, let's begin by first determine a solution with no fixed time. Let us also define our three sampling points (x, y) in vector form.

Define $\mathbf{y} = \begin{pmatrix} y_0 \\ y_1 \\ y_2 \end{pmatrix}$ and $\mathbf{x} = \begin{pmatrix} x_0 \\ x_1 \\ x_2 \end{pmatrix}$. Let $b = b(y_0, y_1, y_2)$ be a function for our exponential parameter.

If the points are distributed accordingly to Eq.4.22, equation 4.25 can be written as:

$$\frac{e^{-x_0b} - e^{-x_1b}}{e^{-x_1b} - e^{-x_2b}} - \frac{y_0 - y_1}{y_1 - y_2} = 0 \quad (4.26)$$

Here to determine the derivative of b , we need the single derivative with respect to each variable. Taking the derivative of the equation with respect to y_0 :

$$\frac{\partial}{\partial y_0} \left(\frac{e^{-x_0b} - e^{-x_1b}}{e^{-x_1b} - e^{-x_2b}} - \frac{y_0 - y_1}{y_1 - y_2} \right) = 0 \quad (4.27)$$

and solving for $\frac{\partial b}{\partial y_0}$ we get:

$$\frac{\partial b}{\partial y_0} = \frac{(e^{x_1b} - e^{x_2b})^2 e^{-(x_0+x_1+x_2)b}}{F} \quad (4.28)$$

where

$$\begin{aligned} F = & x_0y_1e^{x_1b} - x_0y_1e^{x_2b} - x_0y_2e^{x_1b} + x_0y_2e^{x_2b} \\ & - x_1y_1e^{x_0b} + x_1y_1e^{x_2b} + x_1y_2e^{x_0b} - x_1y_2e^{x_2b} \\ & + x_2y_1e^{x_0b} - x_2y_1e^{x_1b} - x_2y_2e^{x_0b} + x_2y_2e^{x_1b} \end{aligned} \quad (4.29)$$

Let's set aside the result of this equation. We will now consider the derivatives with respect to the remaining variables, y_1 and y_2 , though the results will not be displayed as they do not provide additional information to the reader.

Instead, let's assume we have calculated all the derivatives with respect to each variable and evaluate them at the points $y_i = e^{-x_i}$ for $i = 0, 1, 2$, i.e.,

$$\left. \frac{\partial b}{\partial y_i} \right|_{y_i=e^{-x_i}} = f_i(\mathbf{x}, b) \quad \text{for } i = 0, 1, 2 \quad (4.30)$$

If the uncertainties in y_i are attributable to binomial statistics, we can extend Eq.4.8 as follows:

$$\partial y_i = \sqrt{\frac{y_i - y_i^2}{N}} \quad (4.31)$$

Now, assuming we calculated all the terms of $\nabla b(y_0, y_1, y_2)$, we can now determine the total uncertainty on b as a simple error propagation. Let us define the function $\partial b(\mathbf{x})$ as:

$$\partial b(\mathbf{x}) = \sqrt{\sum_{i=0}^2 \left(\left. \frac{\partial b}{\partial y_i} \right|_{y_i=e^{-x_i}} \right)^2 (\partial y_i)^2 \Big|_{y_i=e^{-x_i}}} \quad (4.32)$$

or equivalently in matrix form as:

$$\partial b(\mathbf{x}) = \sqrt{(\nabla b(\mathbf{y}))^2 \cdot (\partial \mathbf{y})^2 \Big|_{\mathbf{y}=e^{-\mathbf{x}}}} \quad (4.33)$$

assuming we represent the gradient ∇ as a row vector. Note that this expression depends not only on the sampling points \mathbf{x} but also on the value of b itself, as seen in the gradient factor (Eq.4.28), and on the number of shots N (Eq.4.8).

To find the optimal point to minimize ∂b , we need to calculate the derivative and set it to 0. Since this has no analytical solution, we solve it numerically. Our goal is to find the minimizing combination of sampling points, meaning we want to place our 3 sampling points so that the error on the parameter b , defined as ∂b , is the lowest. By plotting the optimized function on a cube (Figure 4.8) as a function of the 3 sampling points, we can verify our modeling by observing certain hints. For example, we expect symmetry with respect to each $x_i = x_j$ diagonal, on every face of the cube, which means swapping two sampling points should not affect the final uncertainty. Another hint of correctness is given by looking at the diagonals. Sampling with diagonal elements means two of the three sampling points approach each other, wasting the measure since we already have information about the curve in that area. Diving deeper and changing the scale range of values, we see that our optimized point lies on one face of the cube, not inside it (Figure ??), indicating that one of the optimized sampling points is 0. Further analysis reveals that the other two optimal sampling points are around $1T_1$ and $4.5T_1$. This makes sense as the spacing between the points allows us to fit the curve well and obtain the parameters with minimal uncertainty. Let's now examine how reintroducing the parameter t affects the evolution of the optimized point and the uncertainty.

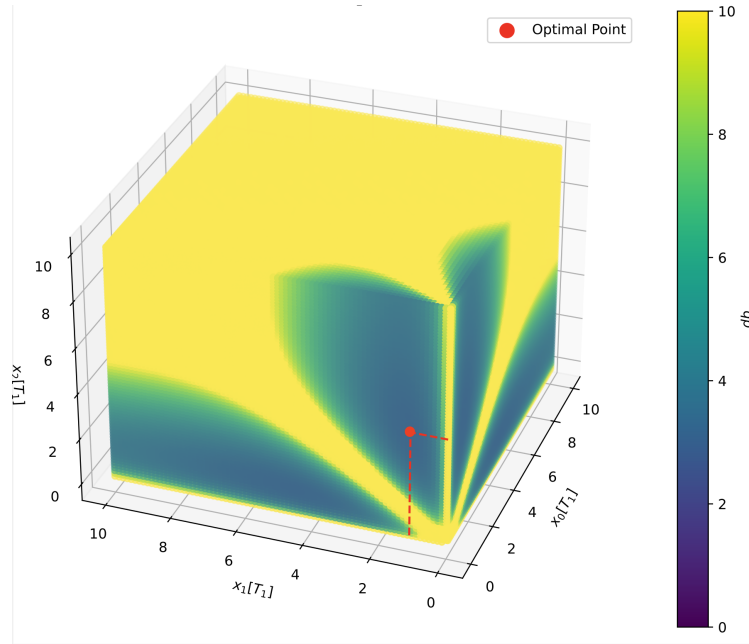


Figure 4.8: Optimized function on a cube as a function of the 3 sampling points, showing the optimal sampling point $\mathbf{x}_{\text{opt}} = (0, 1.091, 4.519)T_1$.

Figure 4.9

4.6.1 Reset Time Case

As already discussed for the 1-point solver, the limit of perfect measurements, i.e. instant measurements, is quite a case limit, seeing no real applications in experiments. To introduce delays given by different factors, such as reset time, or readout time, we again introduce a new parameter t to the equation, which is a generic term for a time delay between one measurement and the other. This time parameter is purely a generic factor, and can include whatever process can be included between following measurements. This time, we have to add the 3 different sampling times, and our substitution reads:

$$T = N \left(\sum_{i=0}^2 x_i + 3 \cdot t \right) \quad (4.34)$$

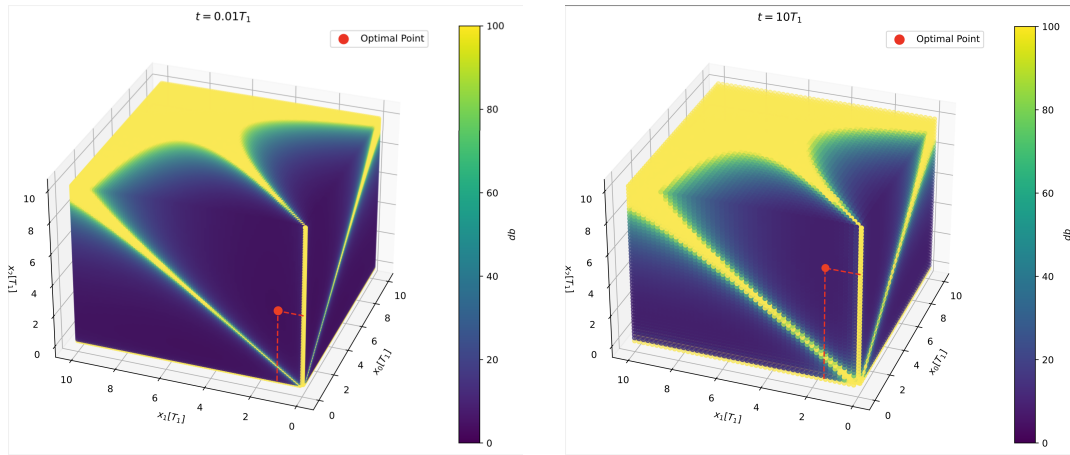
where T is the total experimental time. Then Eq.4.32 can be written considering $y_i = e^{-x_i}$ as

$$\partial b(\mathbf{x}, b, t, T) = \sqrt{\sum_{i=0}^2 \left(\frac{\partial b}{\partial y_i}(x_i, b) \right)^2 \cdot \frac{(e^{-x_i} - e^{-2x_i}) \left(\sum_{i=0}^2 x_i + 3 \cdot t \right)}{T}} \quad (4.35)$$

We now have a comprehensive understanding of how the uncertainty of b scales with the total time T , given three sampling points \mathbf{x} , a reset time t , and the value of b itself, which corresponds to our previously described γ , i.e., the decay rate. First, we aim to determine how the displacement of our sampling points x influences our uncertainty. Specifically, we seek the combination \mathbf{x}_{opt} that minimizes this uncertainty. Again, minimizing this equation does not yield an analytical solution, so it is necessary to solve it numerically. To do this, we observe that we can remove the dependence on T , as it acts as a multiplicative factor. After removing T , we also need to remember that $b = \gamma$ by definition. Additionally, we must fix our most relevant parameter, t . In the following analysis, we will examine different examples with various values of t to compare different decay rate measurement methods.

Let's now analyze the scenarios we discussed earlier for the single point solver, specifically at times $t = 0.01T_1 \equiv t_{\text{reset}}$ and $t = 10T_1 \equiv t_{\text{wait}}$. We observe that the first sampling point remains stationary at zero throughout the cases. The optimal midpoint, which initially starts at $x_{\text{opt},0} \approx 1T_1$ in the reset case (see Figure 4.10a), evolves towards approximately $1.5T_1$ as time progresses to $t \rightarrow 10T_1$ (refer to Figure 4.10b). As illustrated in the sliced cube (Figure 4.12), where each slice is taken at the respective optimal coordinate, the final optimal sampling point $x_{\text{opt},2}$ undergoes a more rapid evolution, shifting from around $5T_1$ to over $8T_1$. To gain a comprehensive understanding of the evolution of our sampling points, we can also examine the trajectory of the optimal point in \mathbb{R}^3 (Figure 4.13). This figure clearly shows that while one coordinate remains constant, the other two coordinates evolve, with one scaling more rapidly than the other.

After determining the optimized sampling points for different cases, \mathbf{x}_{opt} , we can use Eq. 4.35 to calculate the uncertainty associated with these optimal combinations. As expected from the analytical derivation, the scaling of σ_{T_1} over time is consistent with other solutions, reducing the comparison to other curves to an offset. The spacing between the t_{reset} and t_{wait} solutions for the 3-point solver is narrower compared to the same spacing for the single-point solver (figure 4.14). This suggests that the dependence on the parameter t in the 3-point solver is weaker, as the sampling points already occupy most of the time, and adding a waiting time influences the total uncertainty less. Besides comparing the spacing between t_{reset} and t_{wait} , we can also compare the spacing between the 3-point solver solutions and the single-point solver solutions. The



(a) Optimized function on a cube as a function of the 3 sampling points for t_{reset} , showing the optimal sampling point $\mathbf{x}_{\text{opt}} = (0, 1.094, 4.531)T_1$. (b) Optimized function on a cube as a function of the 3 sampling points for t_{wait} , showing the optimal sampling point $\mathbf{x}_{\text{opt}} = (0, 1.5, 7.131)T_1$.

Figure 4.10: Evolution of the optimized function over two different times. (a) shows the cube at t_{reset} , and (b) shows it at t_{wait} .

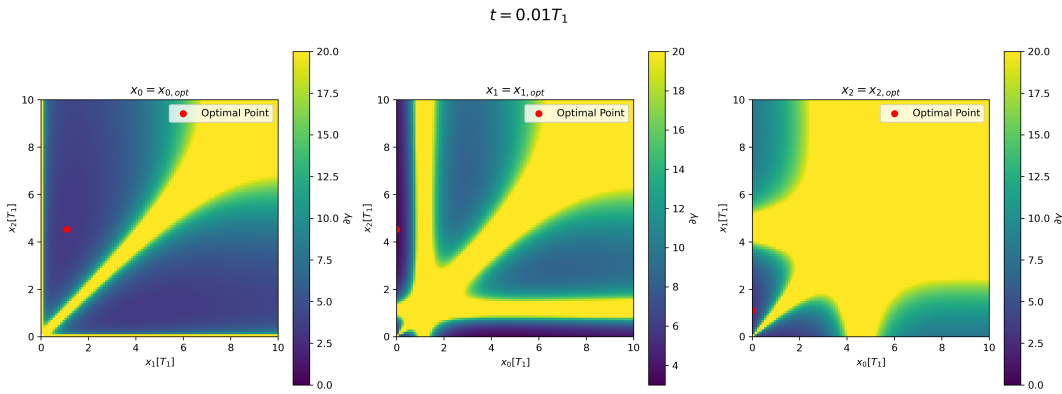


Figure 4.11: Sliced view of the cube at the respective optimal coordinates for t_{reset} , showing the optimal sampling point.

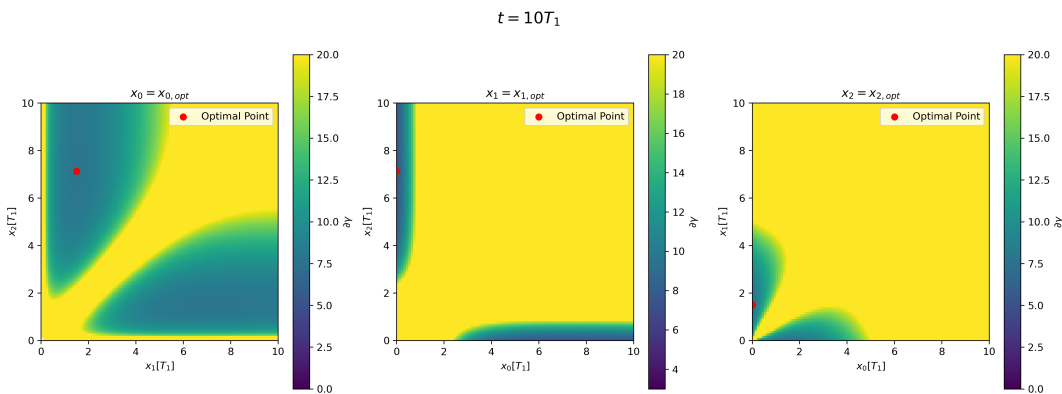


Figure 4.12: Sliced view of the cube at the respective optimal coordinates for t_{wait} , showing the optimal sampling point.

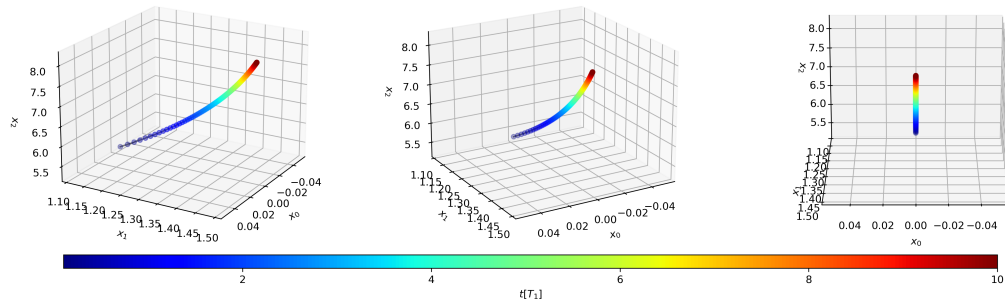


Figure 4.13: Evolution of the optimal sampling point in \mathbb{R}^3 .

former lies significantly above the latter, as achieving the same uncertainty with 3 parameters requires a longer time compared to the single-point solver.

To verify our theoretical solutions, we turned to simulations. However, this time we needed to generate 3 points and use the 3-parameter exponential curve as a reference. This method ensures that our theoretical models are accurately represented and validated through empirical data. While the simulations correctly verify our analytical solutions for all other methods, in the 3-point solution for the t_{wait} case, at shorter timescales, our model seems to deviate from the analytical solution. This could be due to multiple factors. For example, consider the extreme left part of the plot, where the total time is $T \approx 100T_1$. A single optimal T_1 measurement in the t_{wait} case takes $\sum_{i=0}^2 x_i + 3t \approx 40T_1$, meaning that, on average, we can only obtain two values of T_1 , out of which we determine σ_{T_1} —a relatively small sample size for reliable data. This problem also affects the relative error bars, which are calculated using bootstrapping. Since bootstrapping assumes that the original sample is representative of the overall population, if the original sample does not adequately represent the population, as in our case, the bootstrap samples will also fail to capture the true population characteristics. However, in general, for longer timescales, our model remains reliable in all cases, as shown.

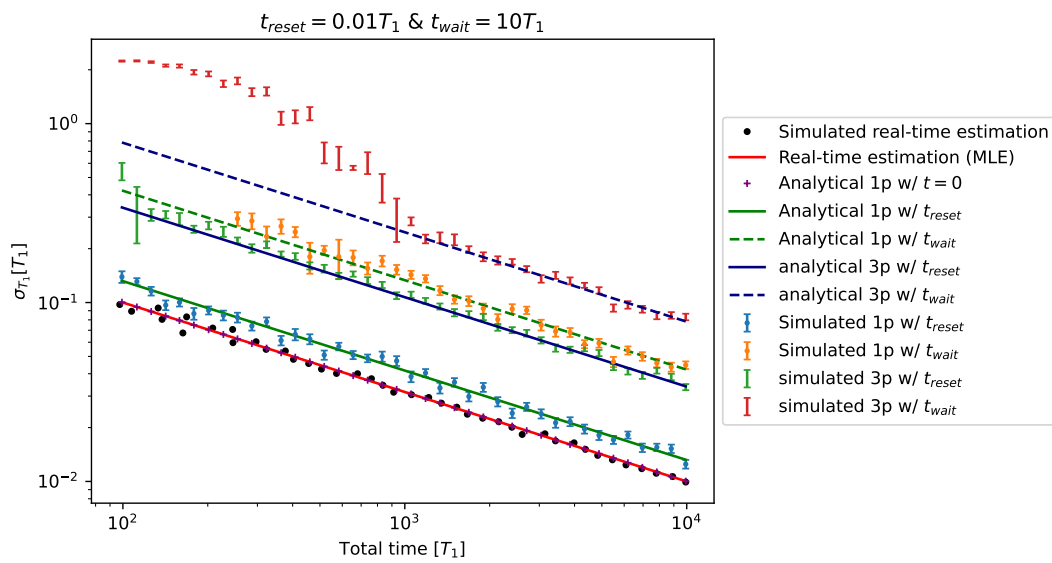


Figure 4.14: Comparison of the uncertainty scaling for different solver approaches over time. The plot illustrates the differences between the 3-point and single-point solvers, particularly in the spacing between t_{reset} and t_{wait} and the overall uncertainty. Note the deviation at shorter timescales for the 3-point solution, likely due to insufficient sampling, as discussed in the text.

Conclusions and Outlook

Throughout this thesis, we have demonstrated both theoretically and numerically how our newly developed method can significantly enhance qubit decay rate measurements. In the initial chapters, we introduced the fundamentals of quantum computing and examined the mechanisms underlying qubit decay and relaxation. To facilitate this understanding, we covered measurement processes applied to two-level systems and explored various operations relevant to qubit dynamics. We then introduced the Lindbladian formalism to describe open quantum system behavior, providing a solid foundation for studying qubit relaxation.

Building on these concepts, the second chapter focused on quantum jumps, which form the core of our novel decay rate measurement technique. We introduced the concept of weak continuous measurements, first in the context of Gaussian variables and later within a Poisson framework to accurately model quantum jumps. Vijay's protocol for continuous quantum jump measurements was also discussed, along with its mathematical underpinning via the Stochastic Master Equation, which enabled us to track the time evolution of a 'jumping' qubit. In addition, we clarified and simulated the analysis required to convert raw measurement data into cleaner signals, highlighting the crucial role of measurement efficiency.

In the final chapter, we presented our new method for achieving the fastest and most accurate decay rate measurements. Through rigorous mathematical derivations, we proposed a novel model and protocol capable of outperforming standard and specialized measurement techniques. Numerical simulations were employed to compare these different methods, thereby quantifying the advantages offered by our approach.

This work opens several promising avenues for future exploration. Further research into continuous qubit monitoring may lead to deeper insights into quantum measurement theory and the development of advanced control proto-

cols. Additionally, integrating machine learning techniques with the methods developed here could enhance real-time analysis and prediction of qubit behavior, ultimately enabling even faster and more precise measurements.

Bibliography

- [1] Carlos Alexandre Brasil, Felipe Fernandes Fanchini, and Reginaldo de Jesus Napolitano. „A simple derivation of the Lindblad equation“. In: *Revista Brasileira de Ensino de Física* 35.1 (Mar. 2013), pp. 01–09.
- [2] Kurt Jacobs and Daniel A. Steck. „A straightforward introduction to continuous quantum measurement“. In: *Contemporary Physics* 47.5 (Sept. 2006), pp. 279–303.
- [3] J.R. Johansson, P.D. Nation, and Franco Nori. „QuTiP 2: A Python framework for the dynamics of open quantum systems“. In: *Computer Physics Communications* 184.4 (2013), pp. 1234–1240.
- [4] A.N. Jordan and I.A. Siddiqi. *Quantum Measurement: Theory and Practice*. Cambridge University Press, 2024.
- [5] Andrew N. Jordan, Areeya Chantasri, Pierre Rouchon, and Benjamin Huard. „Anatomy of fluorescence: quantum trajectory statistics from continuously measuring spontaneous emission“. In: *Quantum Studies: Mathematics and Foundations* 3.3 (May 2016), pp. 237–263.
- [6] P. V. Klimov, J. Kelly, Z. Chen, *et al.* „Fluctuations of Energy-Relaxation Times in Superconducting Qubits“. In: *Physical Review Letters* 121.9 (Aug. 2018).
- [7] P. Krantz, M. Kjaergaard, F. Yan, T. P. Orlando, S. Gustavsson, and W. D. Oliver. „A quantum engineer’s guide to superconducting qubits“. In: *Applied Physics Reviews* 6.2 (June 2019).
- [8] Daniel Manzano. „A short introduction to the Lindblad master equation“. In: *AIP Advances* 10.2 (Feb. 2020).
- [9] Z K Mineev, S O Mundhada, S Shankar, P Reinhold, R Gutiérrez-Jáuregui, R J Schoelkopf, M Mirrahimi, H J Carmichael, and M H Devoret. „To catch and reverse a quantum jump mid-flight“. In: *Nature* 570.7760 (June 2019), pp. 200–204.

- [10] Marco Taboga. „Exponential distribution - Maximum Likelihood Estimation“. In: *Lectures on probability theory and mathematical statistics* (2021).
- [11] R. Vijay, D. H. Slichter, and I. Siddiqi. „Observation of Quantum Jumps in a Superconducting Artificial Atom“. In: *Phys. Rev. Lett.* 106 (11 Mar. 2011), p. 110502.
- [12] Wikipedia contributors. *Bloch sphere* — *Wikipedia, The Free Encyclopedia*. [Online; accessed 27-January-2025]. 2024.
- [13] Wikipedia contributors. *Qubit* — *Wikipedia, The Free Encyclopedia*. [Online; accessed 30-January-2025]. 2025.